GEOCHEMICAL AND NANOPETROPHYSICAL CHARACTERISTICS OF THE HORN RIVER FORMATION: BRITISH COLUMBIA, CA

by

JOSEPH ANTHONY SORTORE

Presented to the Faculty of the Graduate School of

The University of Texas at Arlington in Partial Fulfillment

of the Requirements

for the Degree of

MASTER OF SCIENCE IN

Geology

THE UNIVERSITY OF TEXAS AT ARLINGTON

May 2017

Acknowledgements

I would first like to thank those at the British Columbia Oil and Gas, Robert Story, Mark Hayes, David Edwards, Christine Richards and all other unknown, involved parties for their continued persistence in helping me acquire core samples for the research, without which this project would have not happened. Patrick Russell and Jacqueline Urban of Weatherford Labs Calgary, AB served as intermediaries between me and the lab technicians that plugged the core samples which were shipped to UTA, and their assistance is greatly appreciated.

At UTA I would like to thank Dr. Max Hu for his knowledge and support, and patience during the delayed process of acquiring samples. The rest of my advisory committee, doctors John Wickham and Andrew Hunt, for their participation as well as several recommendations for an internship and scholarships which have helped me to develop professionally.

Lastly to my mother, Lori Sortore, who has always been there to listen, love and support me even when others were not, I am extremely grateful. And my brother, Michael Sortore, who never fails to inspire and uplift others – especially me. And to my closest friends and department colleagues, our jokes, thoughts and conversations, I hope, were of as much benefit to you as they were to me, and I wish you the best of luck in your current and future work as well.

➔ Defense Date: April 21, 2017

Abstract

COUPLED GEOCHEMICAL AND NANOPETROPHYSICAL ANALYSIS OF PRODUCIBILITY IN THE HORN RIVER FORMATION: BRITISH COLUMBIA, CA

Joseph Sortore, MS

The University of Texas at Arlington, 2017

Supervising Professor: Qinhong (Max) Hu

The Devonian Horn River basin of northeastern British Columbia is the largest producing shale gas field in Canada. It has an estimated 500-600 TCF of light hydrocarbons in place stacked in multiple formations in an over-pressured setting conducive to, but too tight for natural flow. Not until the development of new drilling and production technologies were implemented a little over a decade ago were these massive resource plays able to be exploited. Shale development in British Columbia began in 2005 with the Triassic Montney Play, and shortly after that the Horn River Play in 2007. As of 2012, the Horn River Basin comprises 28% of British Columbia's recoverable gas reserves.

However, recoverable gas is only about 15% of gas-in-place, and this phenomenon is the result of rock, pore and fluid characteristics and interactions that restrict the transport of fluid from the pores of the rock matrix, into the natural and induced fracture network and ultimately the wellbore. Research surrounding rock-fluid interactions and dynamics and their relationship with the geochemical properties of the formation is necessary in order to evaluate a reservoir's producibility. Therefore, the

focus of this research is centered on studying pore topology and geochemical correlations and their implications to steep production decline in shale gas wells. Several following experimental methods will be utilized: Video wettability measurements and contact angle measurements to understand the rock-fluid interface, Mercury Injection Capillary Pressure experiments to acquire basic petrophysical properties and assess pore-size distribution and architecture, and a spontaneous imbibition study to measure the uptake of fluids via capillary pressure and assess pore connectivity probability. These together, analyzed along with geochemical data and well logs gathered from the Oil and Gas Commission in British Columbia will be used to interpret the producibility within the Horn River Formation's three members.

Table of Contents

List of Illustrations

List of Tables

Chapter 1

Introduction

In recent years, new drilling and completion technologies have opened up avenues for resource exploitation, and as a result, have created an industry-wide shift in perspective towards discovering how to better produce shale gas. Canada, having over 500,000 oil and natural gas wells and producing 16,495 petajoules of energy in 2010, 41.4% of which was from natural gas, is the 3rd largest producer of natural gas in the world totaling 60,200 bcf in 2012 (Rivard, et al., 2014). Approximately 95% of the natural gas produced in Canada was by conventional means while the rest was either from shales or coalbed methane, unconventionally, totaling approximately 1000 tcf GIP (Ross, 2008; Rivard, et al., 2014). Falling slightly behind the US in terms of utilizing newly developed horizontal drilling and fracturing technologies, their first shale gas production began in 2005 with the Montney Play Trend followed by the Horn River Formation – the subject of this research – in 2007 which are both located in the territory of study, British Columbia (Rivard, et al., 2014). In 2009, the territory accounted for 20% of Canada's total production of (National Energy Board, 2011). British Columbia has four active plays all located in the northeast part of the territory, the Horn River Basin (HRB), Montney Play Trend to the south, and to a lesser extent the Liard Basin to the west and the Cordova Embayment to the east (Rivard et al., 2014). The HRB is up to 320m thick and is estimated to hold 600 TCF of natural gas (Khan, et al., 2012). Thus, much time, research and monetary attention is currently given to discovering more efficient production strategies and addressing the worldwide shale production problems.

The Horn River Formation (HRF) is part of the massive Western Canadian Sedimentary Basin (WCSB), and colloquially represents a set of three different producible shale members, the Evie and Otter Park members of the HRF and the

Muskwa Formation. The WCSB saw its first oil and gas production in 1947 with the Leduc oil field, but today most of its production comes from the HRF (Rivard, et al., 2014). As stratigraphic research progressed, the Muskwa Formation became incorporated as a distinct member of the HRF whereas before it was classified as its own formation (1983, Williams). This research will consider it a member of the HRF. The HRF is part of the HRB and is located in Northeastern British Columbia and Alberta from Figure 1-1. The formation is located on a westward facing coastal shelf setting and represents a period of transgression. To the west it is bound by the Bovie fault, and to the East and South are the time-equivalent Slave Point and Presqu'ile carbonate platforms (Ross and Bustin, 2008).

This project focuses on the petrophysical properties of the Devonian-aged HRF shales, Evie and Otter Park, and the Muskwa shale members which, at their depth, produce mostly dry, sweet gas (>85% methane) with about 10-11% CO_2 (BCOGC Atlas, 2014). The massive basin covers approximately 7,100 mi^2 in northeast British Columbia. The gas shales represent about 21% of BC's remaining gas reserves, and production has been increasing every year to 180 BCF in 2014 (BCOGC Reserves, 2014). Gas in place (GIP) figures due to the inherent uncertainty vary, but are in the range of 145 – 800 TCF. Most figures lie in the 300-450 TCF range and are increasing with time and discovery while the marketable, recoverable gas is generally only 15-25% of that (National Energy Board, 2011). Porosity is generally reported to be in the range of 3-6%, but values as high as 12% have been reported. However, given the low permeability values, in the nano-darcy range, the HRF is a tight over-pressured, dry gas play (Ross, 2008).

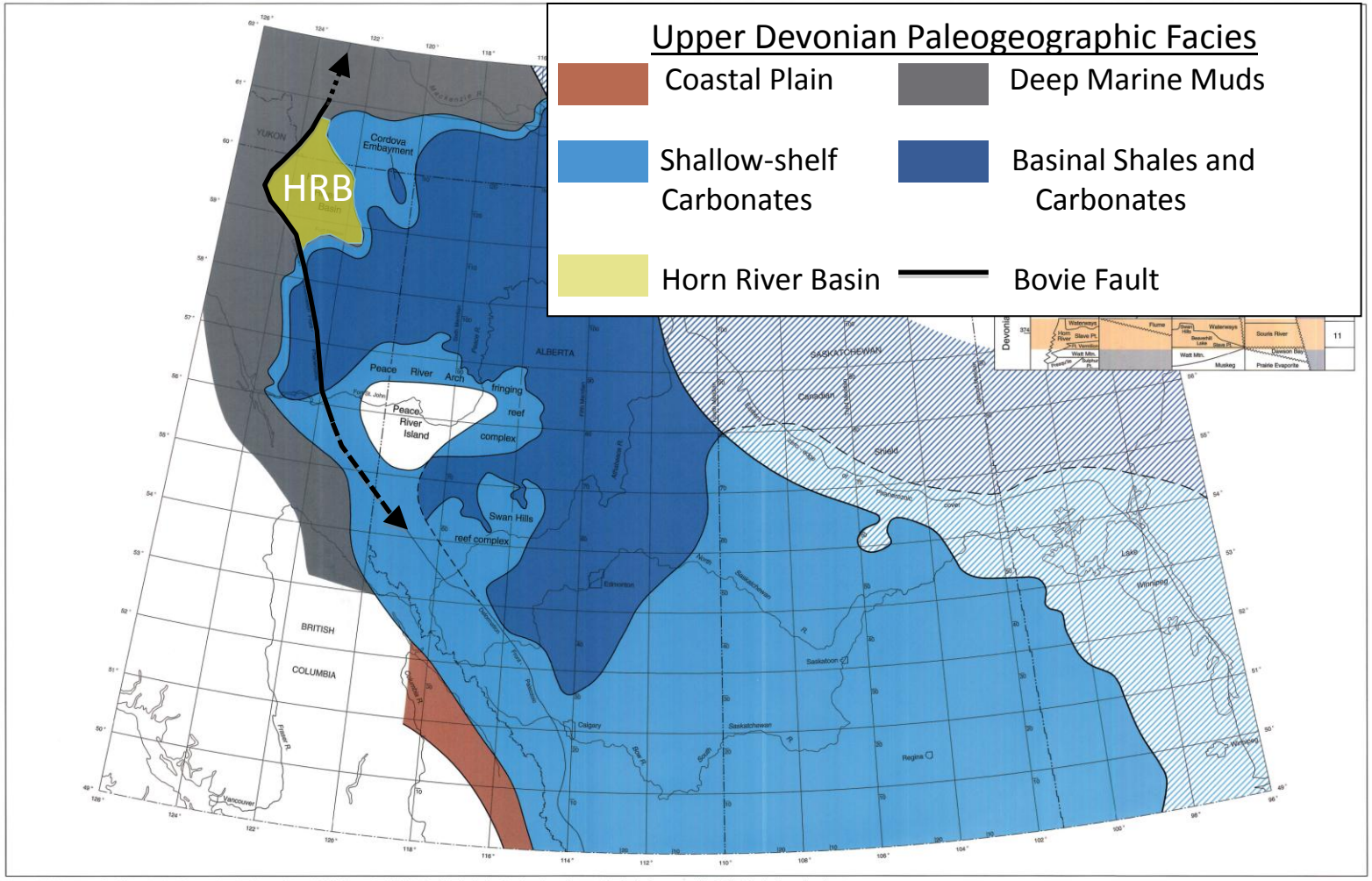

Figure 7.8 Paleogeography of the cratonic platform and margin during subinterval DM3. Fine-grained siliciclastics of the basinal marine deposits are interpreted as having been sourced in the hinterland to the north and east.

Figure 1-1: Devonian paleogeography of Western Canada with the Horn River Basin highlighted in yellow (AGS Atlas, 2016).

These disparities between GIP and recoverable gas are cited as a problematic source among those exploiting the basin's resources as well as the massive body of published research surrounding it. Hu (2012) describes that shale properties vary greatly from basin to basin as well as localities within a basin, and that drilling, hydraulic fracture and completion design should vary to reflect these changes.

The three formations differ significantly in lithology and in pore structure and size. Evie and Otter Park formations show a correlation between TOC and porosity suggesting organic porosity while the Muskwa appears to have a more complex pore network lacking many typical correlations such as mineral-porosity (Harris and Dong, 2013). Poor understanding of matrix structure and thus permeability and the geologic controls which effect such values of these heterogeneous plays is the primary culprit which keeps flow rates low and decline curves steep. Decline rates in several US shale plays average approximately 80-95% in about 36 months (Hu et al., 2015), and these rates exist in the HRB as well. In the Barnett shale of Texas, this issue has left the total gas recovered at only 12-30% as reported in 2012.

Fluid transport in the reservoir depends upon reservoir pressure, pore network geometry, fluid viscosity, effective stress (Chalmers et al., 2012), as well as pore topology that is poorly studied (Hu et al., 2015). All of these factors can be altered during well completion and production. Also, the types of porosity present, intragranular versus kerogen for example, will affect the wettability of the shale with the fluids present (Anderson, 1986). Temperature also affects the wettability of the fluids within the formation, causing imbibition rates and volumes to fluctuate (Hjelmeland and Larrondo, 1986). As temperature increases from low (22°C) to high (above 60°C), the wetting state becomes more water-wet. Lan et al. (2015) discovered significant variations in wettability

values depending on the experimental procedure. While testing solid versus crushed rock samples in the Horn River, they found that solid rock samples had an affinity for water while crushed rock samples had an affinity for oil. Therefore, oil-wet pores in the Horn River samples that were studied were not connected to the sample edge, allowing high water imbibition. Sigal (2008) found that gas diffusion in the advection-diffusion coupled transport mechanism becomes important at ultra-low permeability intervals. Dong and Harris (2013) show that in the Horn River shales, porosity estimates using SEM images were significantly lower likely due to the presence of smaller, sub-resolution pores.

Producibility is then influenced by the shale matrix, controlled by the ratio of sorbed to free gas and the wetting state of the connected matrix which the fracturing fluids are able to contact, and the pore network itself. Flow from the shale matrix to the well bore sequentially involves gas desorption, diffusion and then Darcy flow from disconnected micro- to nano-pores to the larger natural and induced fracture network with a pathway to the wellbore. If hydrocarbons are not in contact with the fracture network, production will inevitably be low leading to large discrepancies in GIP and recovered gas. This project aims at providing a quantified characterization of the Horn River Formation by exploring the geologic and petrophysical controls on producibility in the Horn River Formation.

Chapter 2

Geologic Setting

The WCSB is a massive, resource-rich basin with a surface area of $1.4x10^6$ km^2 spanning 5 different territories, Manitoba, Saskatchewan, Alberta, British Columbia and the Northwest Territory and containing numerous world-class oil and gas fields. It is bounded on the east by the Canadian Shield and on the west by the Canadian Cordillera and is subdivided into the northern Alberta Basin and southern Williston Basin – which are further sub-divided into smaller sub-basins. The Horn River Basin is contained within the northern Alberta Basin. Its development began during Late Proterozoic, and it has a sedimentary record dating back to Lower Paleozoic times, approximately 450 Ma while the youngest rocks preserved are approximately 53 Ma (Mason, 1994).

The basin's development occurred in 2 major tectonic stages which greatly influenced both the provenance and lithology of the roughly 6000m of sediment recorded: 1) a rifting stage which became a passive margin adjacent to an ocean basin to the west of the North American craton; and 2) a foreland basin stage accompanied with the growth of the Cordilleran mountain belt and the Canadian Rocky Mountains (Mossop and Shetsen, 1994). The passive margin saw deposition of carbonates and carbonaceous shales while the foreland basin saw the deposition of mainly conglomerates, sandstones and shales (Mason, 1994). The HRF was deposited during the former stage.

The members of interest for this work, the Evie, Otter Park and Muskwa shales, are Devonian in age and are members of the 370 mya Horn River Formation of the WCSB. The Horn River basin is an embayment on a westward facing coastal shelf. Shown in Figure 2, the basin is bounded on the west from the Liard basin by the Bovie normal fault system. Across the Bovie Fault, which underwent slip during Permian-

Carboniferous crustal uplift and the Late Cretaceous Laramide orogeny, strata displacement is nearly 1,200 m separating the Liard and Horn River basins (Ross and Bustin, 2008; MacLean, 2004). Here, the foreland basin stage sandstones and conglomerates in the Liard Basin are juxtaposed against the passive margin carbonates and shales (Leckie, 1992). To the East-Northeast and South of the Horn River Basin, shallow water carbonates of the Slave Point and Presqu'ile platforms form its eastern and southern boundary. Westward of the Slave Point platform, the deep-water, time-transgressive shales of the Horn River group are found and east of the platform lays the Cordova Embayment. The Muskwa shale is the uppermost member of the organic rich shales of the Horn River basin (Figure 3). It ranges in thickness from approximately 60 m near the Bovie fault to only about 5 m on the basin margins (Levson, 2009). Below that, the Otter Park formation reaches a maximum thickness of about 270 m in the southeast corner and the Evie member, which is the thickest near the carbonate reef towards the east, reaches approximately 75 m (National Energy Board, 2011).

The Horn River group comprised of the three shale units listed above overly the Keg River carbonates. Overlying the uppermost member, the Muskwa shale, is the massive (up to 1000 m in some locations), calcareous Fort Simpson shale formation followed by the Red Knife formation.

Sequence stratigraphically, the sediment package between the Lower Keg River formation up through the Red Knife formation represents two 2nd order cycles with a maximum flooding surface at the Muskwa formation leaving it farther offshore than the carbonates which bound it above and below. TOC values from McPhail et al. (2008) of the Horn River

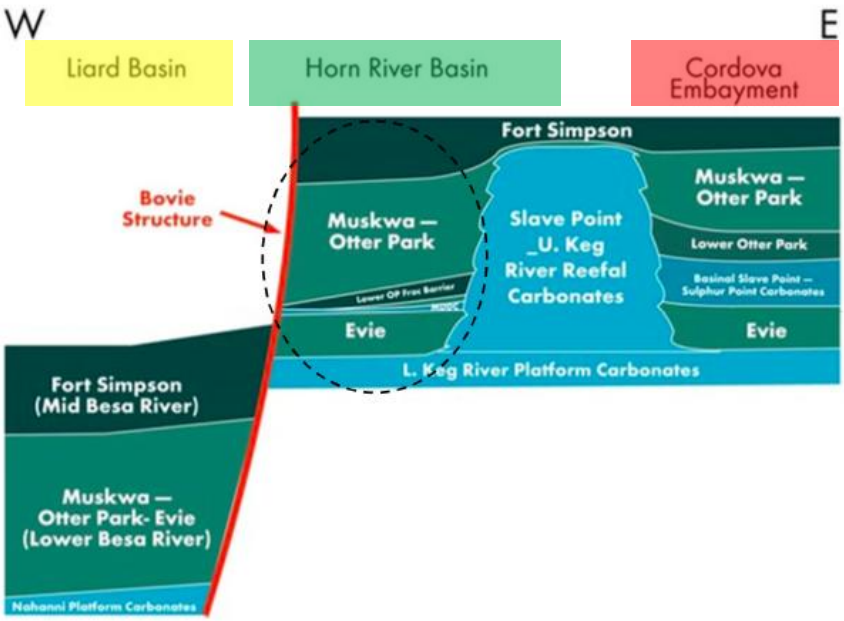

Figure 2-1: Cross-section across the Liard and Horn River Basins (National Energy Board, 2011).

			Liard Basin		Horn River Basin		Platform
Devonian	Upper	Frasnian	Besa River Formation	Fort Simpson Formation	Fort Simpson Formation		Fort Simpson Formation
				Muskwa Fm	Muskwa Fm		Muskwa Fm
	Middle	Givetian		Horn River Fm: Otter Park Member	Horn River Fm	Otter Park Member	Slave Point Fm
							Watt Myn Fm
							Sulphur Point Fm
				Horn River Fm: Evie Mbr		Evie Mbr	Upper Keg River Fm
				Dunedin Fm	Keg River Fm		Lower Keg River Fm

Figure 2-2: Stratigraphic Column of the Liard, Horn River and Carbonate Platform (modified after Ferri et al., 2011).

shales range from 0.3-9.6% in the Evie, 1.6-8.0% in the Otter Park and 0.2-5.9% in the Muskwa. The Muskwa member, however, has a relatively high average TOC value of 3.1%, with lower values corresponding to transitional zones of the carbonates above and below it (Levson, 2009). Thermal maturity R_o is relatively high in the range of 2.2-2.8%, well within the dry gas window (National Energy Board, 2011).

Like the Barnett, the Muskwa Formation is a true shale and is actually a fine-grained mud (Nieto, 2009). Lithologically, the Muskwa shale is a very fine-grained, siliceous mudstone containing about 52% quartz, 28% illite/mica, 8% kaolinite, 5% pyrite, 4% carbonates and 3% feldspars in Figure 5 (Harris, 2013; Hall, 2011) and Table 1 (from Lan, et al., 2015). EOG Resources, a primary operator in the basin, has discovered areas where Muskwa shale lithology is up to 85% quartz. Some facies contain radiolarian deposits and pyrite crystals while others lack significant fossil presence and exhibit pyrite streaks evident of weak bottom currents. From Table 2-1 and Reynolds (2010), the lower Evie and Upper Muskwa have significant mineralogical differences. Clay content decreases with depth while pyrite and calcite increase with depth.

Table 2-1: Formation Mineralogy obtained by XRD. Adapted from Lan, et al (2015).

Shale	Quartz (%)	Chlorite (%)	Calcite (%)	Dolomite (%)	Illite (%)	Plagioclase (%)	Pyrite (%)
Muskwa	36.7-60.0	4.4	0	5.2	48.3	3.6	1.7
Otter Park	43.6	0	12.9	2.2	33.8	4.4	3.2
Evie	52.0	0	13.3	3.1	19.2	6.1	3.6

Table 2-2: Compilation of petrophysical values from various literature sources.

Unit	Depth	TOC (%)	Porosity (fraction)	Permeabilty nD)	Source
Muskwa	1792	3.91	0.070		Lan et al. (2015)
Otter Park	2639	3.01	0.090		
Evie	2679	4.10	0.060		
Muskwa	1758	3.91	0.270	35	
Otter Park	2639	3.01	0.270	32	
Evie	2678	4.10	0.270	30.000	
Muskwa			0.036	8.000	Ross (2008)
			0.010	3.100	
			0.023 - 0.066		Dong and Harris, 2013

Chapter 3

Methods

3-1 Sample Procurement and Preparation

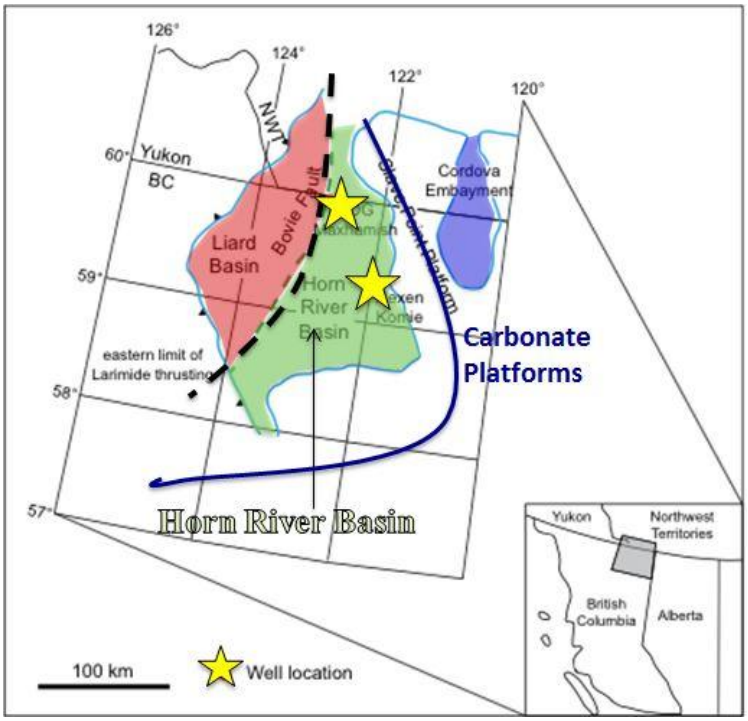

Figure 3-1: Well and Basin Locations (modified from Ross and Bustin, 2008)

The samples used for this project were taken as plugs from slabbed cores of two wells in Northeastern British Columbia. The plugged intervals were picked in high TOC areas according to work done by Dong et al. (2014). The wells are located between 59°N and 60°N and 122°W and 123°W, which encompasses most of the Horn River Basin including its depocenter. Table 3-1 is a list of well and sample names along with their corresponding depths. There are 4 core plugs taken vertically from the 2/3 sections of the 2 slabbed cores and 2 chunks of core sent from sections where the shale was too fissile to plug. They were obtained from the *Core Research Facility* operated by the British

Columbia Oil and Gas Commission (BCOGC) and plugged by Weatherford Laboratories in Calgary, Alberta and inventoried into the *Center for Collaborative Characterization of Porous Media* (C3PM) at the University of Texas at Arlington (UTA), Figures 3-2 and 3-3.

Table 3-1: List of Well and sample names and locations.

Well Name	WA#	Coordinates (Latitude/ Longitude)	Sample Name	Formation	Depth (m)
IMP Komie	24577	59*11'48.87"/ 122*14'19.59"	BC24577MK	Muskwa	2268
			BC24577OP	Otter Park	2277
			BC24577EV	Evie	2386
ECOG Maxhamish	21643	59*55'52.54"/ 122*53'33.26"	BC21643MK	Muskwa	2972
			BC21643OP	Otter Park	3036
			BC21643EV	Evie	3056

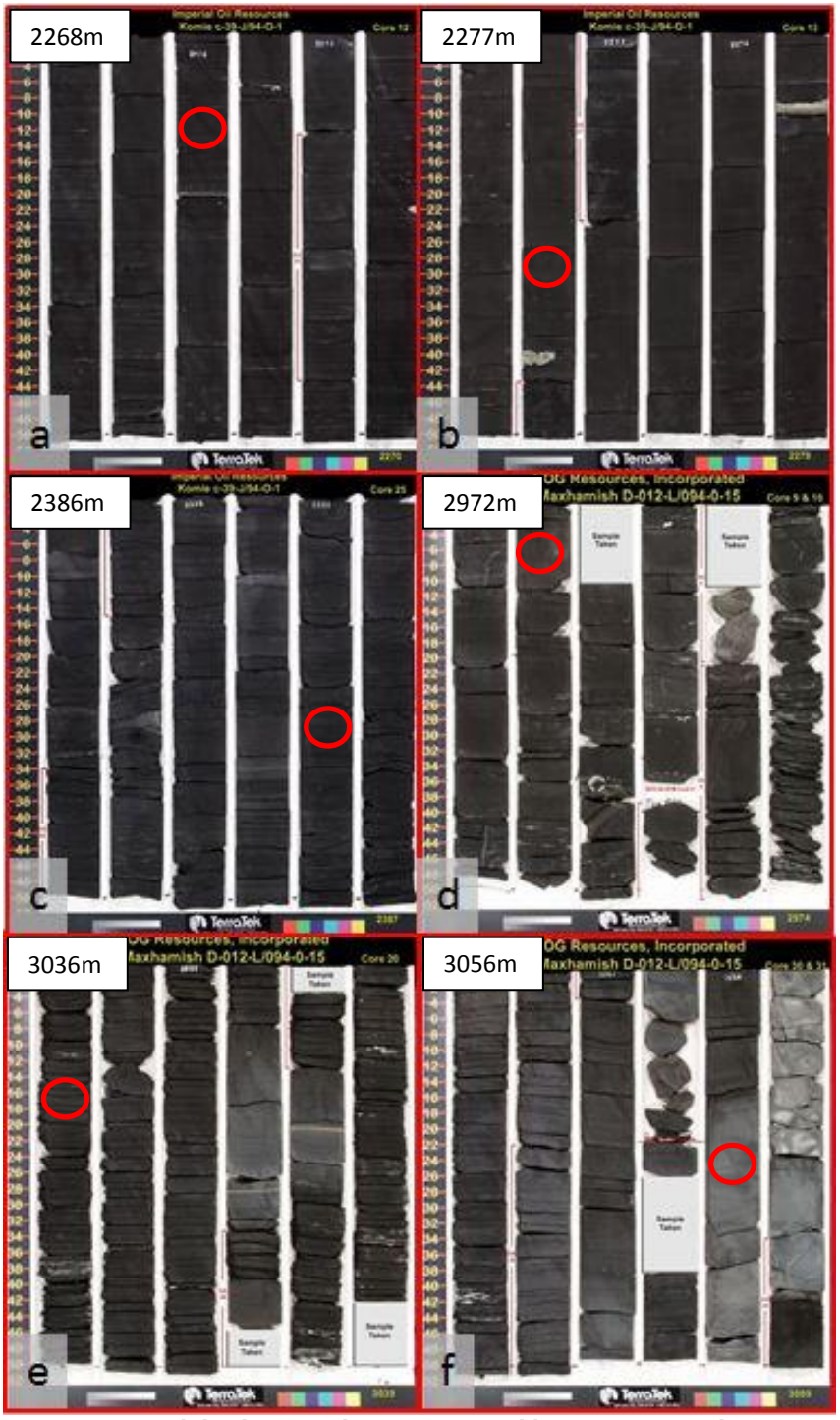

Figure 3-2: Core slab photos: a)BC24577MK, b)BC24577OP, c)BC24577EV, d)BC21643MK, e)BC21643OP, f)BC21643EV

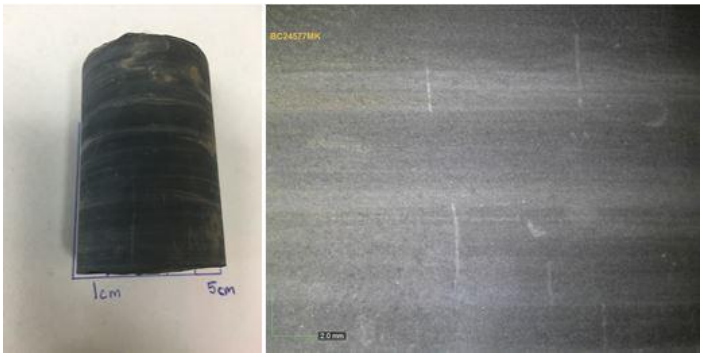

a)

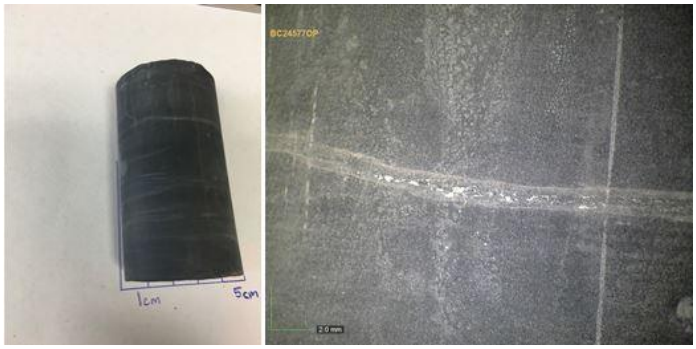

b)

c)

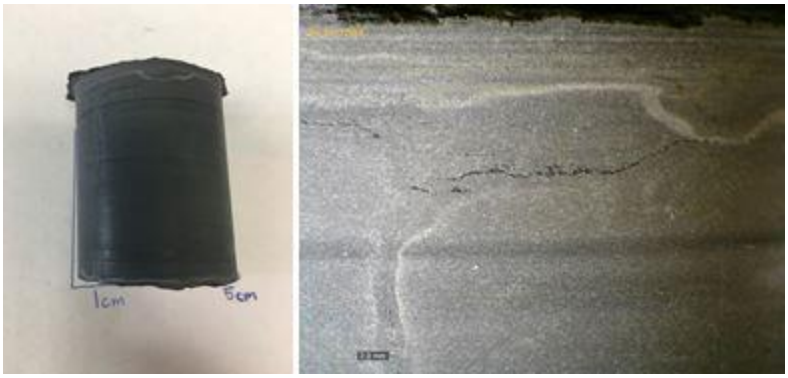

d)

e)

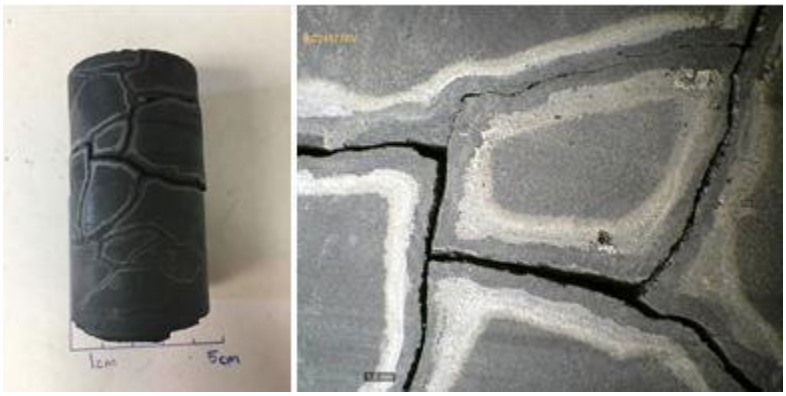

f)

Figure 3-3: Core plug photos (whole and zoomed): a)BC24577MK, b)BC24577OP, c)BC24577EV, d)BC21643MK, e)BC21643OP, f)BC21643EV

Samples were prepared for 4 sets of experiments: 1) Qualitative Wettability, 2) Contact Angle Measurements, 3) Mercury Intrusion Capillary Pressure (MICP), and 4) Imbibition. For qualitative, video wettability and contact angle measurements, small (approximately 1x1 cm) slabs were cut about 2-3 mm thick and polished smoothly. For imbibition, core plugs were cut into 1 cm cubes (Figure 3-4) and subsequently epoxied on the 4 faces perpendicular to bedding. MICP samples were taken from the left-over cuttings after the cubes were prepared.

Figure 3-4: Sample Image of Cubes prepared for Imbibition.

3-2 Wettability and Contact Angle Measurement

The composition of organic rich shales greatly affects the behavior at the rock fluid interface. Reservoir wetting characteristics in turn greatly affect the ability to

efficiently recover oil and gas resources from a low permeability formation. Production from unconventional plays therefore relies heavily on developing accurate methods of determining the wetting characteristics of porous media. A comprehensive review of the various techniques and methods are summarized by Thyne (2013). Two methods were used in this project, a qualitative measurement of wettability and a quantitative measurement of contact angle. Contact angle and wettability have an inverse relationship where $\theta_c \sim \frac{1}{W_i}$. As in Figure 3-5, as θ approaches zero, the fluid is favorably wets the solid's surface.

In the qualitative measurement, we expose the flat, polished surfaces of the sample to fluids with varying compositions and rank the interaction at the interface between 1 and 10 where 1 is completely water-wetting and 10 is completely oil-wetting. The fluids used are DI water, a solution of 1% Isopropyl Alcohol (IPA) and 99% DI water,

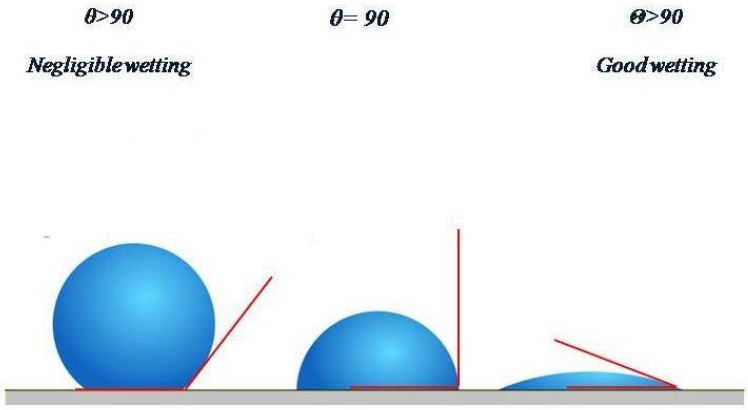

Figure 3-5: 3 cases of fluid/solid interactions.

API brine – a solution of DI water and sodium/calcium salts -- used to emulate saline formation water, and n-decane. Using a 2 μL droplet from a pipette to wet the rock's

surface, an over-head, high resolution video was recorded for 30 seconds to observe the behavior. Video frames at zero, one, ten and thirty seconds were taken to do a drop shape analysis of the spreading behavior for each fluid.

3-3 Mercury Intrusion Capillary Pressure (MICP)

MICP is a test which introduces the non-wetting fluid mercury to the sample at incrementally higher pressures. This pressure dependent invasion of pores causes progressively smaller pore throats to be invaded as the capillary pressures needed to invade them are surpassed. This step-wise pressurization of mercury allows mercury pressures and corresponding intrusion volumes to be recorded; and via the Washburn equation (1921), these values are converted into pore throat diameters. Equation 3-1 below describes Washburn's relationship of mercury pressures to pore throat diameters:

$$\Delta P = -\left(\frac{2\gamma cos\theta}{r}\right) \quad \text{3-1}$$

Where,

ΔP – Change in mercury pressure applied to the sample (psia);

γ – Surface tension for mercury (dynes/cm);

θ – Contact angle between the porous medium and mercury (degrees);

r – Corresponding pore throat radius (μm).

Hu and Ewing (2014) and Kaufmann (2010) have used this step-wise mercury intrusion to create pore distribution curves to understand the morphology and potential sources (inorganic or organic) of the pores present (Hubbert, 2015). The pressures applied have an upward limitation of 60,000 psi (≈414 MPa) which can intrude pore throats as small as 2.8 nm in diameter (Kuila, 2012). Hubbert (2015) also noted that beyond this 2.8 nm threshold, other techniques, such as FIB-SEM, must be used to account for and image

smaller pores. Measurements that are directly gathered included the sample's bulk density, porosity, pore surface area, and pore throat size distribution (Hu et al., 2015). Indirect, topological measurements, permeability and tortuosity can also be indirectly gathered. Permeability is calculated via the Katz-Thompson (1987) equation detailed below.

$$k = \frac{1}{89}(Lmax)^2(Lmax/Lc)\Phi S(\mathrm{Lmax}) \quad \text{..... 3-2}$$

Where,

k = absolute permeability (μm^2)

Lmax = pore throat diameter where hydraulic conductivity is at its maximum (μm)

Lc = pore throat diameter at the threshold pressure

S = is the mercury saturation at Lmax

Tortuosity can be calculated via Equation 3-3 (Hager, 1998; Webb, 2001).

$$\tau = \sqrt{\frac{\rho}{24k(1+\rho V_T)}\int_{\eta=r_c,min}^{\eta=r_c,max}\eta^2 f_v(\eta)d\eta} \quad \text{..... 3-3}$$

Where,

p = mercury density (g/cm^3)

V_{tot} = total pore volume (mL/g)

$\int_{\eta=r_c,min}^{\eta=r_c,max}\eta^2 f_v(\eta)\,d\eta$ = pore throat volume probability density function

The machine used in the laboratory to conduct these MICP experiments was the Micrometrics Autopore IV 9510. Before the samples are placed in the chamber, they are dried at 60°C for 24-48 hours to remove any residual moisture. They are then cooled to room temperature and placed in a dessicator at low, <10%, relative humidity for 30 minutes or until cooling as completed. The sample is then placed into the penetrometer appropriate for the rock type, sealed and placed in the low pressure chamber in the Micrometrics apparatus. The pressure is then reduced to 99.993% vacuum conditions to fully remove air and moisture from the pore system. The sample chamber is then filled with mercury up to a pressure of 30 psi and transferred to the high pressure chamber. Here the pressures are incrementally increased – with an equilibration time of 45 seconds – to 60,000 psi before mercury extrusion begins.

3-4 Spontaneous Imbibition and Vapor Adsorption

Imbibition is the process by which a non-wetting fluid infiltrates a porous medium and displaces the wetting fluid currently present. Morrow (1994), Andersen (2014) and other researchers have cited this as an industry relevant process of recovering oil by [spontaneous] imbibition in conventional plays as well as a major source of fluid loss to the formation. If imbibition occurs spontaneously, it is then a capillary pressure driven process (Ma, 1999; Xie, 2001). Previous work has shown that aside from wetting characteristics, topological parameters play an important role in the advancing wetting front (Ewing and Horton, 2002). Hu (2000) quantifies sorptivity, which is controlled by both capillary pressure and permeability, as the rate of imbibition. This time dependent process of cumulative imbibition is given by Philip (1957) as: $I(t) = St^{0.5} + At$ where I(t) is cumulative imbibition (m), t is time (s), S is the sorptivity ($m/s^{0.5}$), and A is an empirical constant that depends upon the fluid and medium properties and boundary conditions. If flow is horizontal or capillary pressure >> gravity then the term, *At*, is negligible.

Our imbibition experiments utilize percolation theory to determine the probability of the pore and/or fracture network in the samples to be connective. Percolation theory, as briefly summarized by Ewing and Horton (2002): in a geologic medium, a coordination number of bonds (in our case, pores) exists, but only a fraction of them are active or connected. There exists a probability, p_c or percolation threshold, directly above which fluid transport across the body is barely possible. As p increases, the likelihood of the pore network to be connected increases. Well above p_c, the diffusion distance is limited only by the sample size and the distance traveled is proportional to $t^{0.5}$. At or near the percolation threshold it is likely the fluid can only travel along the length of the disconnected, infinite clusters and the displacement is proportional to $t^{0.26}$. In imbibition as with diffusion, in a connected pore network, the distance to the wetting front increases with the square root of t ($t^{0.5}$) within a connected porous medium.

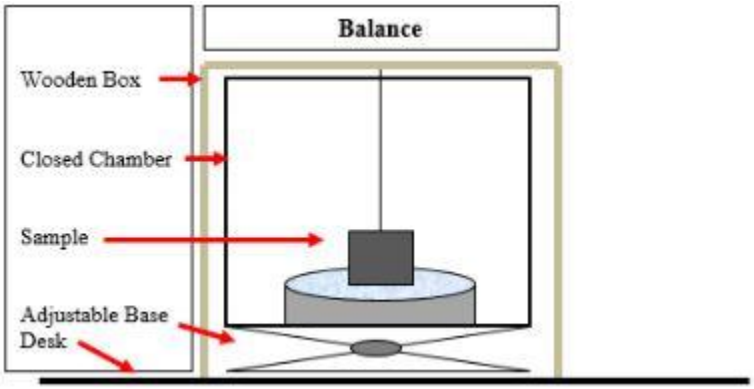

Figure 3-6: Schematic of the Imbibition/Vapor Adsorption Apparatus.

The cubic samples prepared by the method previously described were dried at 60°C, allowed to cool to room temperature and introduced to a chamber that contained a petri dish filled with the fluid, either DI water or n-Decane, used for the experiment. Figure 3-6 shows the sample hanging from the bottom of a highly accurate balance (Shimanzu AUW220WD which has a precision of 0.00001 g and lowered until its bottom face is in

contact with the fluid reservoir. At this point a timer is started and a computer connected to the balance begins logging the sample's weight at pre-specified intervals. Several check weights are taken before and after the experiment. Beforehand, the sample holder, the sample alone, the holder and sample together and the fluid-filled petri dish are weighed. Afterwards, a DI water-wet kim wipe before and after wiping the sample, the holder and sample together, the sample alone, the holder alone and the fluid-filled petri dish are weighed. Data are then processed to remove to primary sources of error, the influence of buoyant forces and the evaporative loss of the fluid in the petri dish. Vapor adsorption experiments are conducted exactly like imbibition except the sample's bottom face is hung directly over the fluid rather than in contact with it. These accessory experimental runs are meant to negate the effects of the artificial weight gain induced by the surface tension of the reservoir fluid applied to the bottom sample face and remove buoyant forces.

3-5 Pyrolysis and Geochemistry

In the resource analysis and reservoir characterization of unconventional plays, the integration of multiple datasets is necessary to bring what are at first sight, dull, homogeneous rocks into a new light (Ness et al., 2010). According to Tissot and Welte (1984), all shales worldwide contain some measure of organic content, and the worldwide average of TOC is approximately 0.8 wt. %. Yet not all shales produce oil or gas at or even near economic levels. The true intricacies of these clastic source rocks are found through correlation of multiple datasets.

In combination with petrophysical data gathered on-site, Rock-Eval pyrolysis, XRD, ICP-MS and digital well logs were obtained from the BCOGC and ExxonMobile. Core petrophysical studies are thus far our method of probing the connectivity of pore

networks in shales. However King et al. (2015) and other groups have begun realizing that by correlating petrophysical data that is so diagnostic of pore topology with other datasets gathered, a more complete picture of pore architecture can be formed. As kerogen is matured and oil and gas generation begin, these fluids begin to expel and replace the formation water. It is therefore an important aspect of shale studies to understand not only the values of porosity, permeability, TOC, etc., but to also understand where these exist and in which phase (King et al., 2015; Passey, 1990). As these tests were conducted by other laboratories, Weatherford Labs and TerraTek, the methods used can be found in Appendices A and B.

3-6 Well Log Analysis

Correlating smaller nanometer to centimeter laboratory data with open hole wireline tools at the scale of several feet, a well log model tied with core and thin sections was built. There are 3 primary components in this model of a dry gas reservoir: rock matrix, organic matter, and pore fluids (Figure 3-7), a model consistent throughout the decades (Philippi, 1968; Nixon, 1973; Meissner, 1978). Their dynamic interaction is essential to understanding not only how hydrocarbons are stored but also how they are transported through the rock. As the maturation of the source rock increases, kerogen is converted into liquid hydrocarbons which displace the currently present fluids. Some of the oil will migrate as maturation progresses, and the remaining fluids will crack into methane and its byproducts which are detectable by open-hole logging tools.

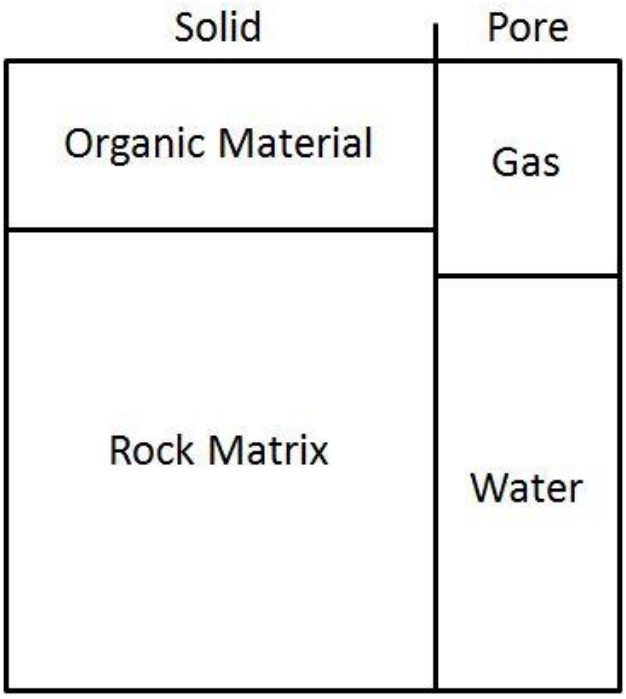

Figure 3-7: Generalized model of a mature source rock

Available to both wells was a full suite of standard logs, and well #24577 had sonic travel time in addition. After formation tops were picked, core data, TOC, mineralogy, and porosity values, was uploaded and plotted in their respective tracks. To match log-derived effective porosity and TOC to core data, a shale corrected porosity log was built. Using the ΔlogR method created by Passey (1990), TOC logs were created and calibrated to core data. In Figures 5-7 through 5-9, the model is displayed. Subsequent core interpretations were used to derive a set of features and cut-off values to establish to most potential pay zones.

Chapter 4

Results

4-1 Wettability and Contact Angle

Table 4-1 Images of Wettability Tests and Relative Wetting Rating (1-10 Wet).

Wettability Test Results					
Well/ Sample		DI Water	API Brine	1% IPA	n-Decane
Maxhamish	BC21643MK			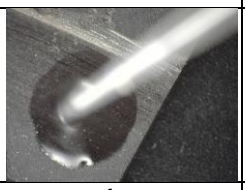	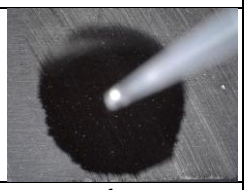
		1s	1s	1s	1s
				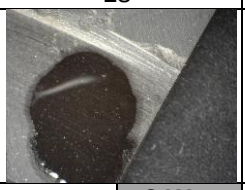	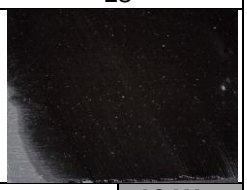
		10s **3 Wet**	30s **4 Wet**	30s **3 Wet**	30s **10 Wet**
	BC21643OP		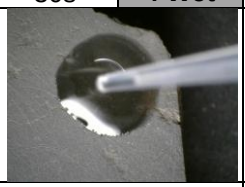		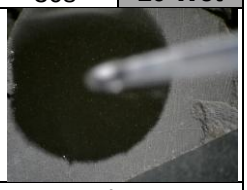
		1s	1s	1s	1s
		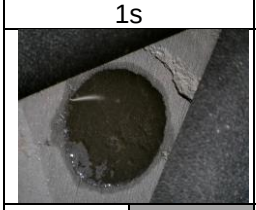	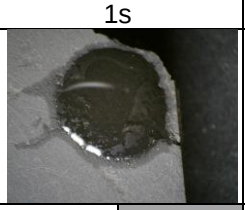	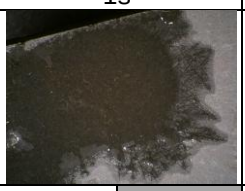	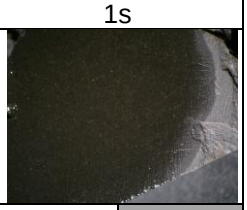
		10s **3 Wet**	10s **3 Wet**	10s **4 Wet**	10s **9 Wet**
	BC21643EV	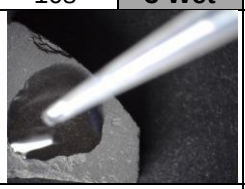			
		1s	1s	1s	1s

		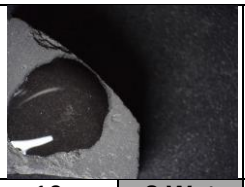	10s	**2 Wet**		10s	**3 Wet**	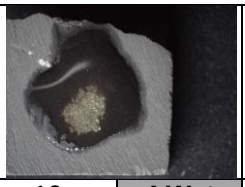	10s	**4 Wet**	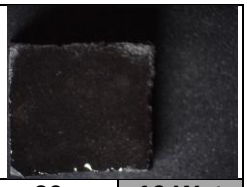	30s	**10 Wet**
Komie	BC24577MK	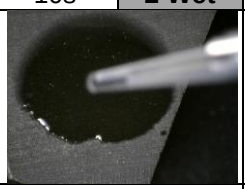	1s		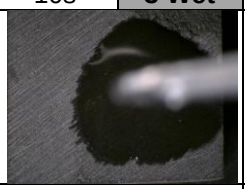	1s		N/A				1s	
		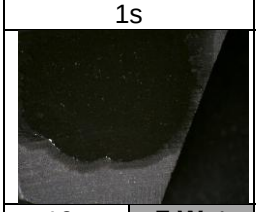	10s	**7 Wet**	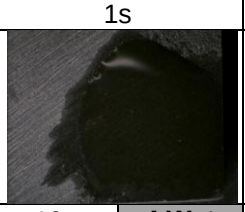	10s	**4 Wet**	N/A				10s	**10 Wet**
	BC24577OP		1s		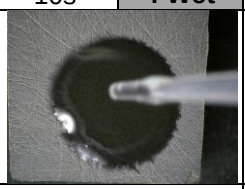	1s		N/A				1s	
		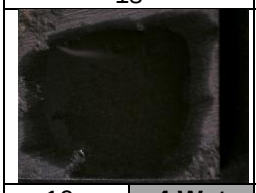	10s	**4 Wet**	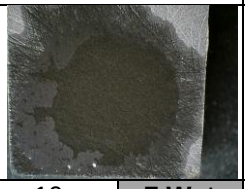	10s	**7 Wet**	N/A			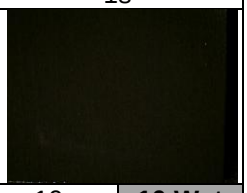	10s	**10 Wet**
	BC24577EV		1s			1s		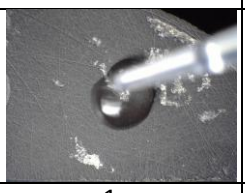	1s		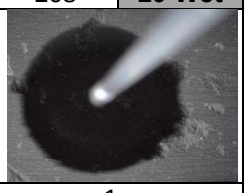	1s	
		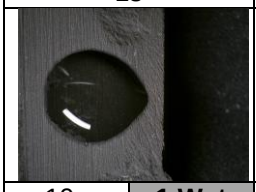	10s	**1 Wet**		10s	**1 Wet**		10s	**1 Wet**	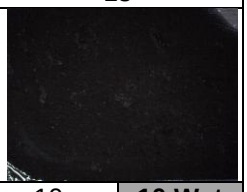	10s	**10 Wet**

Table 4-1 is a compilation of the droplet wettability tests conducted containing the photographs of each sample's surface and a wetting rating on a 10 point scale. On two samples, BC24577MK and BC24577OP, 1% IPA tests were not done. A general trend throughout the samples presents itself while also clearly diverging in one sample. The wettability rating from left to right in the chart increases in each sample and exhibits a preferentially oil wetting surface as can be expected from hydrocarbon bearing source rocks. DI water ratings fall between 1 and 4 with one sample at 7. This unusually large value may be related to its high clay content or organic contact at the polished surface. While API Brine is also typically low, the wetting front of BC24577OP is shown to grow well beyond the droplet. N-Decane for all samples has a high spreading value of 9 or 10. In several samples, notably BC21643MK and BC21643OP, fluid can be seen infiltrating small fractures. It is the abundance of these fractures that make the Muskwa member such a lucrative target in the formation.

Figure 4-1: Contact angle trends decrease (wettability increases) as fluid becomes more rich in hydrocarbons.

Figure 4-1 shows the expected and resultant trend when comparing the contact angles of the fluids used. DI water is near 90° while n-Decane approaches 0°. Several samples shown in Figure 4-2, c, e, and f, deviate from the trend. Samples c and e have large values for API brine and IPA while appearing more water wet. This appears to contradict wettability images from Table 4-1. While sample f has a high value for API

brine, it is validated by corresponding wettability values. All n-Decane measurements show a near zero or below detection limit result due to the surface's affinity for oil. Several factors play a part in these discrepancies and deviations from the results expected.

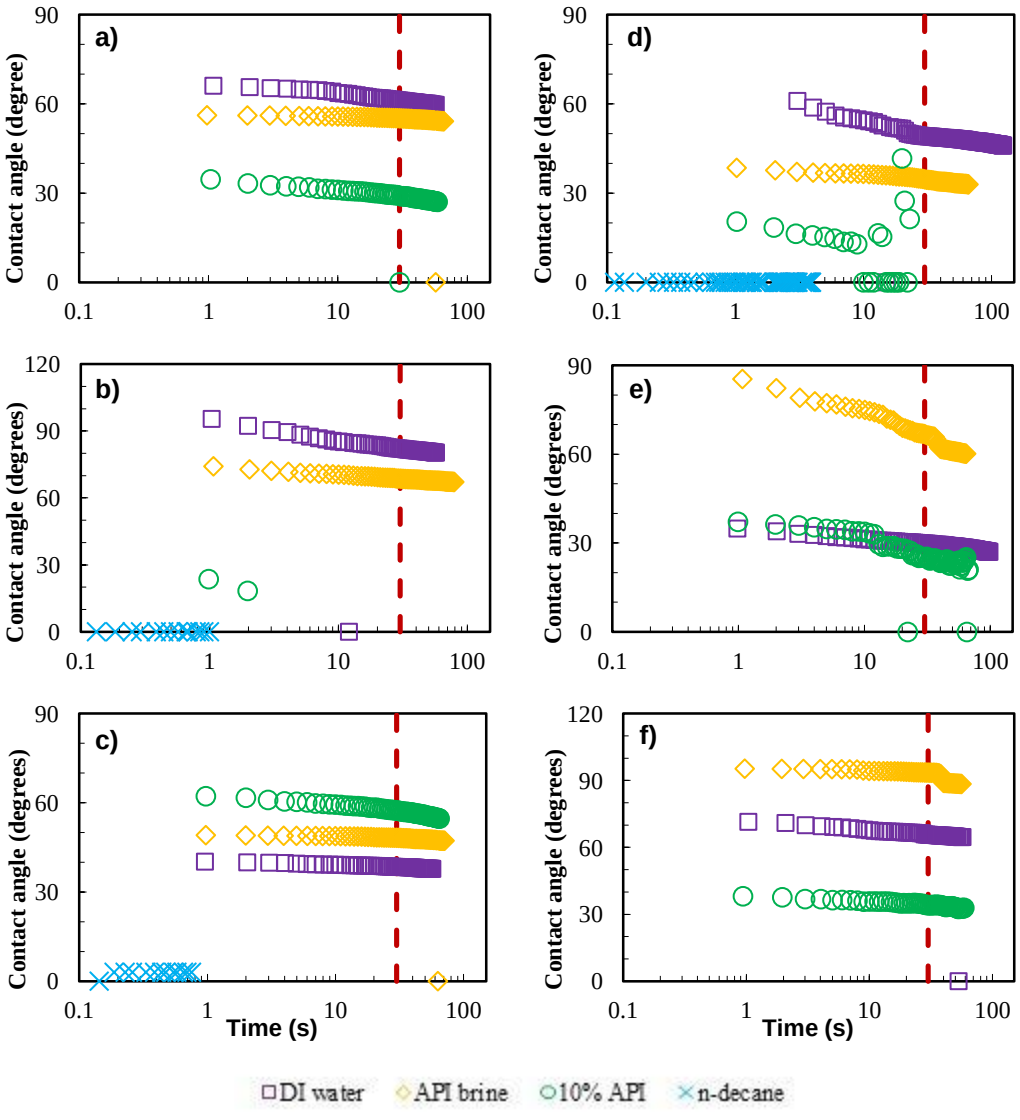

Figure 4-2: Contact angle measurements. a) BC21643MK, b) BC21643OP, c) BC21643EV, d) BC24577MK, e) BC24577OP, f) BC24577EV

Table 4-2: Table of average contact angles in each sample.

Sample ID	DI Water (degrees)	API Brine (degrees)	20% IPA (degrees)	n-Decane (degrees)
BC21643MK	61.64	55.11	28.93	4.75
BC21643OP	82.12	68.64	18.3	<3
BC21643EV	38.42	48.2	57.39	6.03
BC24577MK	49.03	34.62	21.29	<3
BC24577OP	29.89	66.83	25.37	5.48
BC24577EV	65.61	93.52	34.02	3.67

Lower contact angles and higher apparent wettability in non-Decane fluids could be the result of 1) the presence of and affinity of the fluids to clay or 2) pores and throats lacking a hydrophobic coating of hydrocarbons. Conversely, traditionally high contact angles and lower apparent wettability in non-Decane fluids could be the result of 1) the lack of sufficient clays in contact with the surface or 2) a well-connected network of oil-wetting pores.

4-2 Mercury Intrusion Capillary Porosimetry (MICP)

MICP was used to gather primary, indirect petrophysical values for evaluation, porosity, permeability and tortuosity, as well as direct measurements of architectural features: pore throat sizes, pore volume and bulk density.

Table 4-3 below displays the results gathered. All of the samples tested have throats smaller than 3 nm (between 2.7-3.0 nm) suggesting not only that a majority of them exist in organic material, but that a portion of the pore throats remain undetected

due to instrument limitations. Shown below in Figure 4-3, the average of pore throats between 2.7 and 5 nm in size across all samples totals 40.4% of all pore throats.

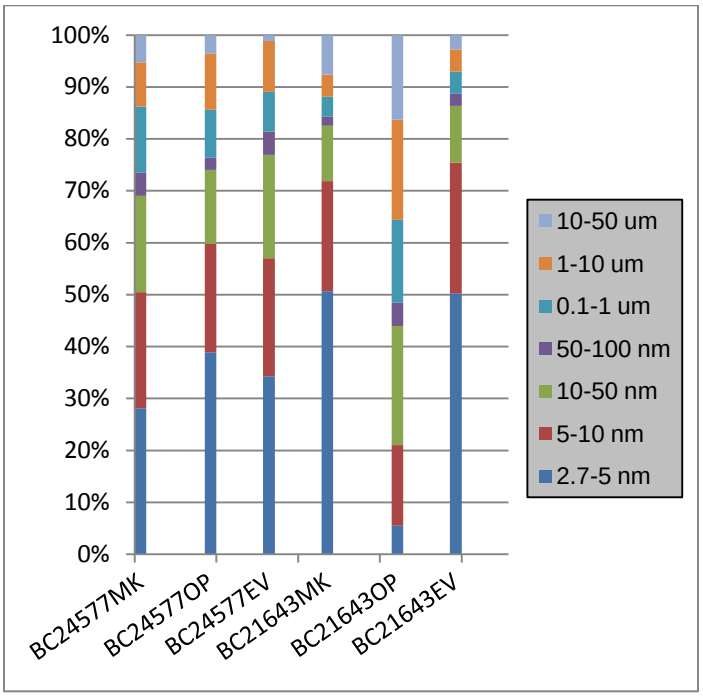

Figure 4-3: Pore-throat Size Distribution

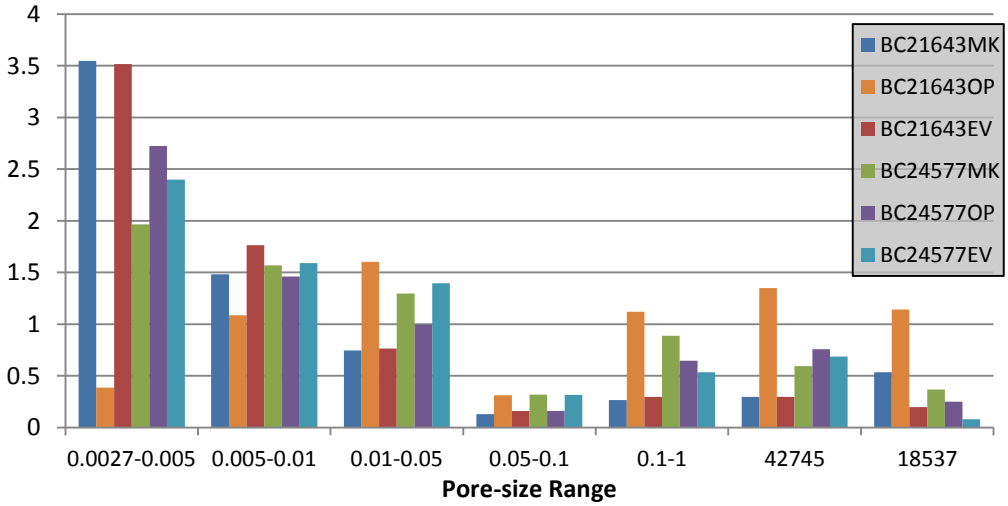

Figure 4-4: Cumulative, Normalized Throat-size Distribution

That percentage decreases with increasing throat size with the exception of throats between 0.1 and 10 um in diameter. The Muskwa member, the primary target in the area, consistently has the highest values of permeability. Although compared to permeability values in conventional reservoirs, these values are considerably smaller and range from 1.34 – 3.51 nD. Tortuosity, as a measure of the degree of non-linearity of the pathways in the sample, is also very high. With the exception of sample 21643OP which shows considerably larger pore throat sizes and permeability.

A statistical analysis of the MICP results reveals several noteworthy trends within the data. Figure 4-4, a non-dimensionalized representation of pore throat-size distribution shows that while throat size is generally smaller in all of the samples, there exists a bimodal distribution of smaller and larger sizes which is likely the result of their various sources of porosity (ie: intergranular porosity, organic or clay porosity). However, the standard deviation of pore volume and surface area is 5 to 7 times greater than the deviation in pore throat diameter suggesting that there is very little correlation between the size of a pore throat and the pores which it connects. This has been reinforced by Passey, et al. (2010) and Hubbert (2015), and it is a likely that the uniformity of throat sizes implies that they have similar geologic origins and reside in similar pore types within the rock. Porosity and both pore volume and area expectedly have a >93% correlation while porosity and pore throat diameter have a strongly (~74%) negative correlation. As pore throats become smaller the sample porosity increases suggesting that samples with higher porosity have smaller throats. Both permeability *k* and tortuosity τ have a negligible relationship to throat diameter but an 84% correlation with themselves, and as such have equally weak yet not negligible relationships to pore area and volume which increase along with both k and τ.

Table 4-3: Summary of MICP Results

	21643MK	21643OP	21643EV	24577MK	24577OP	24577EV
Total Pore Volume (cm^3/g)	0.0126	.0061	0.0084	0.0069	0.0094	0.0072
Total Pore Area (m^2/g)	9.648	1.463	6.755	3.690	5.976	4.280
Median Throat Diamter (Area)	0.0036	.0059	0.0036	0.0040	0.0038	0.0041
Average Throat Diameter (4V/A)	0.0052	.0166	0.0050	0.0075	0.0062	0.0068
Bulk Density (g/cm^3)	2.422	2.4051	2.4449	2.539	2.5887	2.4298
Porosity (%)	3.0488	1.4601	2.0633	1.7583	2.4258	1.7552
Pores Less Than 3nm?	Yes	Yes	Yes	Yes	Yes	Yes
Harmonic Mean for k (nD)	3.51	423.26	1.36	2.59	1.77	1.34

4-3 Imbibition and Vapor Adsorption

Fluid flow in shales and other porous media is generally controlled and therefore characterized according to its porosity, permeability, tortuosity and distribution of pore sizes (Bear, 1972). Geologic consequences which produce the given pore structure in rock are both geometric and topologic, and in low porosity and permeability rocks, topologic factors begin to outweigh geometric factors (Ewing and Horton, 2002). As stated previously, percolation theory is used to describe the connectivity in these rocks (Ewing and Horton, 2002; Stauffer and Aharony, 1994). The wetting front according to percolation theory in previous studies was empirically found to progress with the square-root of time in connected pore systems and approximately the 1/4 power of time in less connected systems (Hu et al., 2012). Hu (2012) ascribes a pore connectivity probability to these imbibition rate slopes.

Table 4-4 contains a summary of slopes from imbibition and vapor adsorption tests obtained from the linear regression of log-log plots of cumulative imbibition over time. N-Decane lab tests produced negative slopes irrelevant to the samples themselves, and therefore those runs were not fully completed. In shale samples, two predominant slopes arise with a typically concave transition zone between them (Yang, 2015). Slope 1 tends to occur within the first 30 seconds to 1 minute of the experiment and ranges from 0.537 to 6.127. Slope 3 occurs within the first hour until the end of the experiment and ranges from 0.089 to 0.553. Slope 1 corresponds with the exposed sample face's initial contact with the fluid surface or vapor. As predicted by percolation theory, there exists an edge accessible porosity which decreases with the distance from the edge of the sample. These are composed of non-connected, finite clusters of pores much like the dead ends of culdesacs. These surface-bound pores create the high initial slope 1. Also according to Yang (2015), the Young-Laplace equation says that smaller pore-throats have higher

capillary pressures and are entered first. As these are disconnected, this also contributes to the rapid decline of slope 1 as it transitions into slope 3.

Table 4-4: Imbibition slopes over time in 2 HRB wells. Water tests were conducted over 3 different time intervals, 6, 12, and 24 hrs.

Sample ID	Experiment ID	Slope 1	Slope 3
BC21643MK	DI Water 6hrs	0.627	0.139
	DI Water 12 hrs	6.127*	0.133
	DI Water 24 hrs	0.537	0.111
	n-Decane 8 hrs	4.084	0.530
	Vapor DI Water 3 d	2.544	0.499
	Vapor n-Decane 1 d		
BC21643EV	DI Water 6hrs	0.642	0.054
	DI Water 12 hrs		
	DI Water 24 hrs	1.001	0.192
	n-Decane 8 hrs		
	Vapor DI Water 3 d	3.502	0.422
	Vapor n-Decane 1 d		
BC24577MK	DI Water 6hrs	0.617	0.163
	DI Water 12 hrs	2.970	0.096
	DI Water 24 hrs	1.850	0.124
	n-Decane 8 hrs		
	Vapor DI Water 3 d	1.520	0.553
	Vapor n-Decane 1 d		
BC24577OP	DI Water 6hrs	0.924	0.089-0.210
	DI Water 12 hrs	0.660	0.241
	DI Water 24 hrs	0.813	0.160
	n-Decane 8 hrs		
	Vapor DI Water 3 d	1.726	0.539
	Vapor n-Decane 1 d		

*Slope 1 anomalously high due to water's high interfacial tension

As the wetting front advances to the inner section of the sample, accessible porosity declines and the slope in the imbibition porosity profile declines (slope 3).

Figures 4-7 through 4-12 are the graphs of log imbibition over time. As shale source rocks are typically mixed to oil wetting, we see water imbibition test results which have low, 0.089-0.241, slopes indicative of a poorly connected pore network. The n-Decane run completed has a slope of 0.530 as samples preferentially imbibe oil into the high count of organic pores present in them. Closer analysis of each imbibition profile

shows several potential fractures. Figures 4-7A shows a spike and relaxation of the profile. Several samples also become convex near the end of the run suggested the wetting front has reached the top face of the sample. Several anomalously high slope 1's occurred. These values are likely artifacts of the interfacial tension between the two media. As water has a high surface tension and the samples are not all equally lowered into the fluid reservoir, there is an artificial weight gain associated with slope 1 in the DI water experiments that is not necessarily an indicator of high or low edge accessible pore connectivity.

Vapor adsorption data return consistently higher values for both slope 1 and slope 3. Slope 1 values range from 1.520-3.502 while slope 3 values range from 0.422-0.533. These higher slopes which are indicative of a better connected network of pores, when juxtaposed against imbibition values in the same sample, may have several causes which are extraneous to pore network connection. 1) Vapor molecules are smaller than liquid molecules, and each invades a pore by different means. A vapor molecule will condense inside of a capillary tube (pore throat) once the meniscus of the condensate is less than or equal to the diameter of the pore throat (Kiepsch, 2016). 2) A recent study has found that the vapor and fluid phases can exist together in nano-porous samples, and that at a relative humidity above 0.6, capillary condensation triggers imbibition within the sample (Vincent et al., 2017). 3) All vapor tests were conducted after imbibition tests. As such, fractures may have been induced by abundant swelling of clay minerals that increased the connection between pores.

When comparing these results to literature findings, there is a stark contrast between the expected and resultant volumes of each fluid imbibed. Contact angle findings in the Horn River shales suggest that the surfaces (and likely the interior) of the samples are oil wetting. It follows that imbibed fluid volumes would reflect this trend.

However, in Figure 4-5, it is shown that the samples imbibe significantly more water than they do n-Decane. Lan (2015) found that by crushing Horn River samples and then conducting imbibition experiments, they became more oil-wetting. It is likely that the organic and inorganic pore networks are significantly disconnected in the Horn River, and that the organic network is further disconnected from open fluid migration pathways. Figure 4-6 is an SEM image from the Horn River displaying this potentiality.

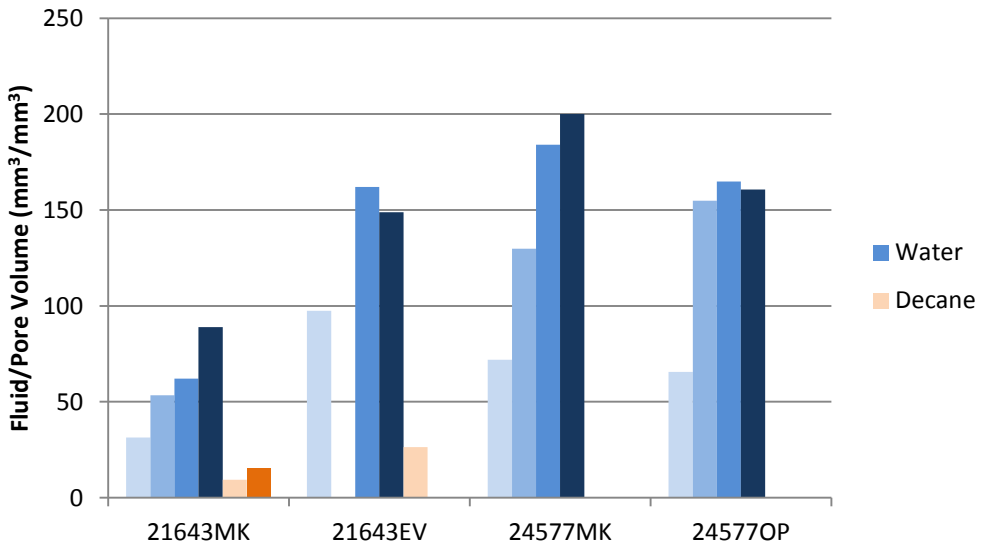

Figure 4-5: Volume of fluid imbibed. Blue = DI water tests and Red = n-Decane tests

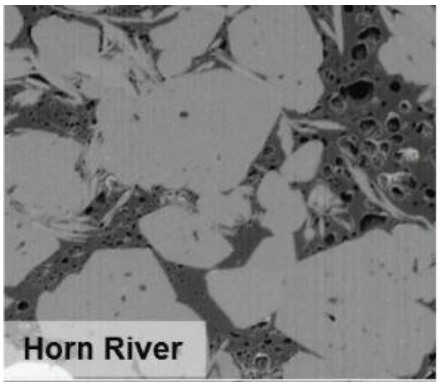

Figure 4-6: Backscattered electron (BSE) image displaying disconnected organic pores (black) in the Muskwa member (modified from, Curtis, 2010).

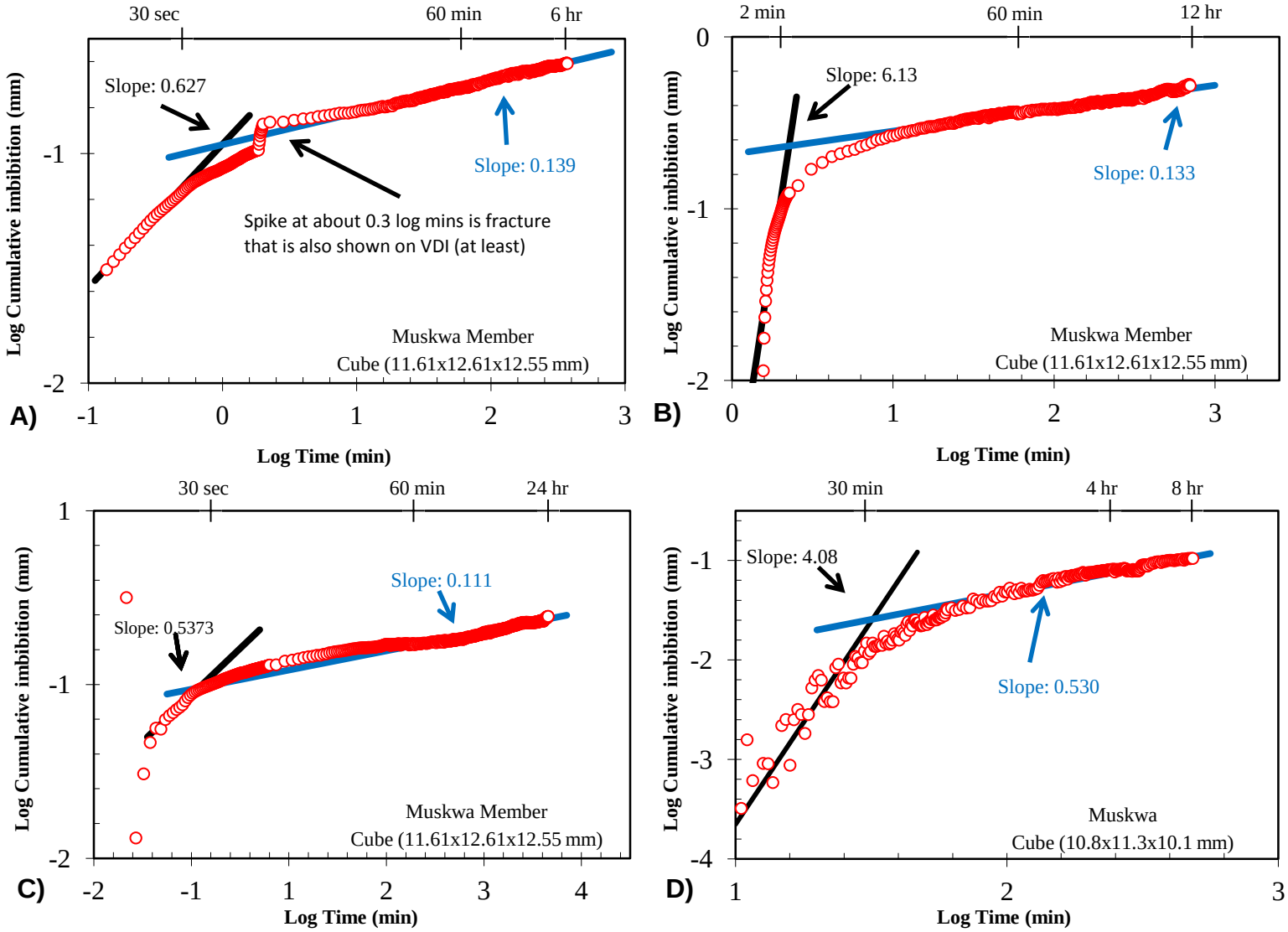

Figure 4-7: Imbibition curves for BC21643MK. A) 6 hr. DI water, B) 12 hr. DI water, C) 24 hr. DI water, D) 8 hr. n-Decane

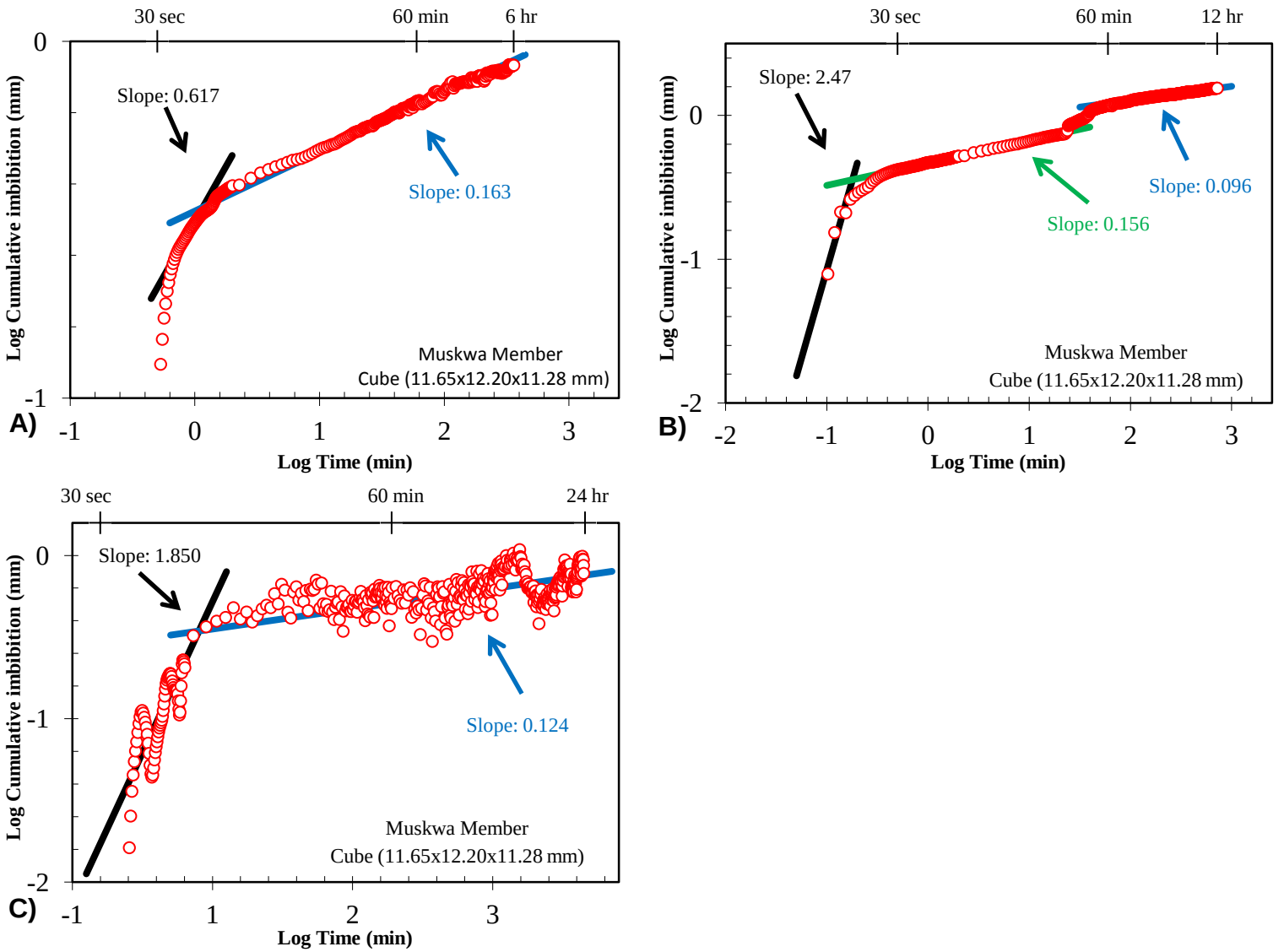

Figure 4-8: Imbibition curves for BC24577MK. A) 6 hr. DI water, B) 12 hr. DI water, C) 24 hr. DI water, D) 8 hr. n-Dec

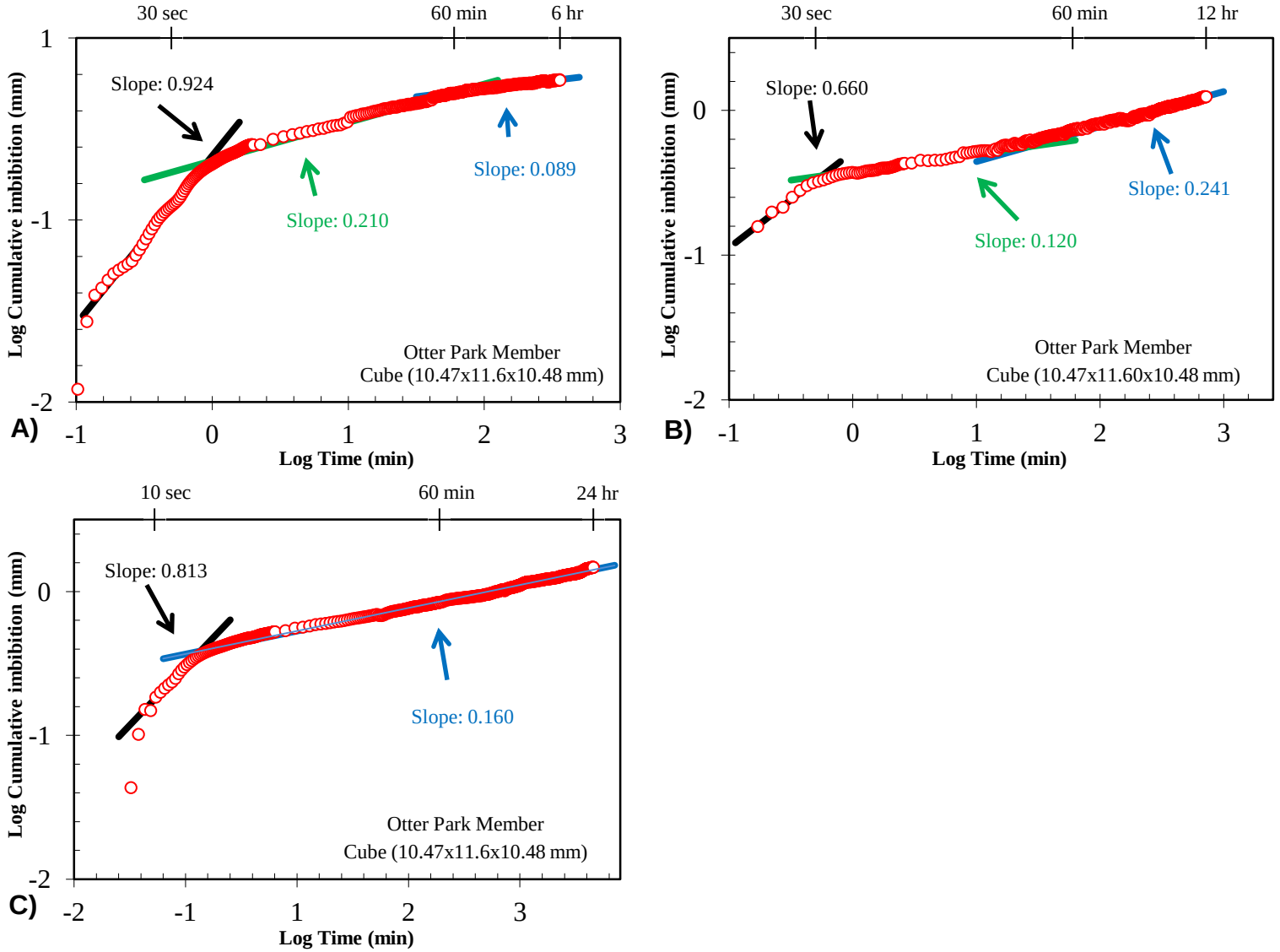

Figure 4-9: Imbibition curves for BC24577OP. A) 6 hr. DI water, B) 12 hr. DI water, C) 24 hr. DI water, D) 8 hr. n-Decane

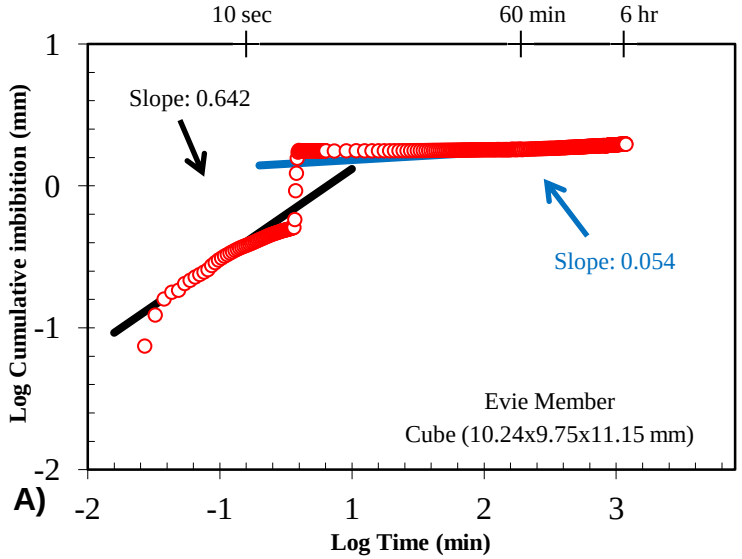

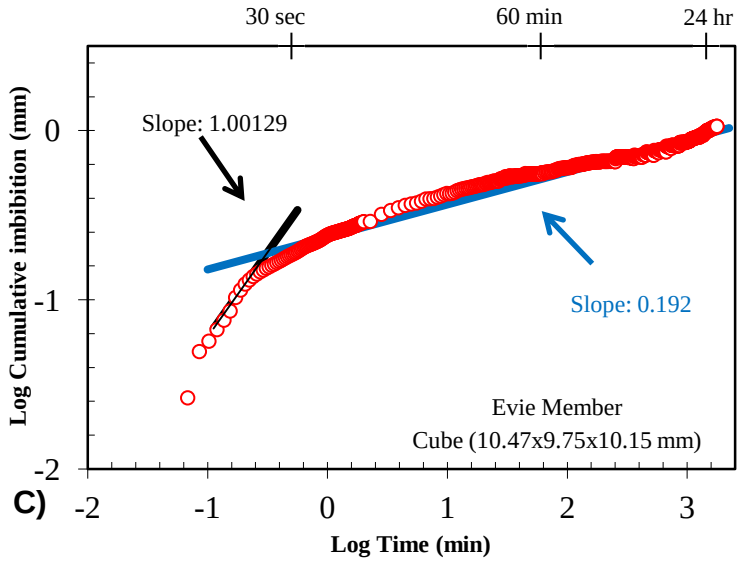

Figure 4-10: Imbibition curves for BC21643EV. A) 6 hr. DI water, B) 12 hr. DI water, C) 24 hr. DI water, D) 8 hr. n-Decane

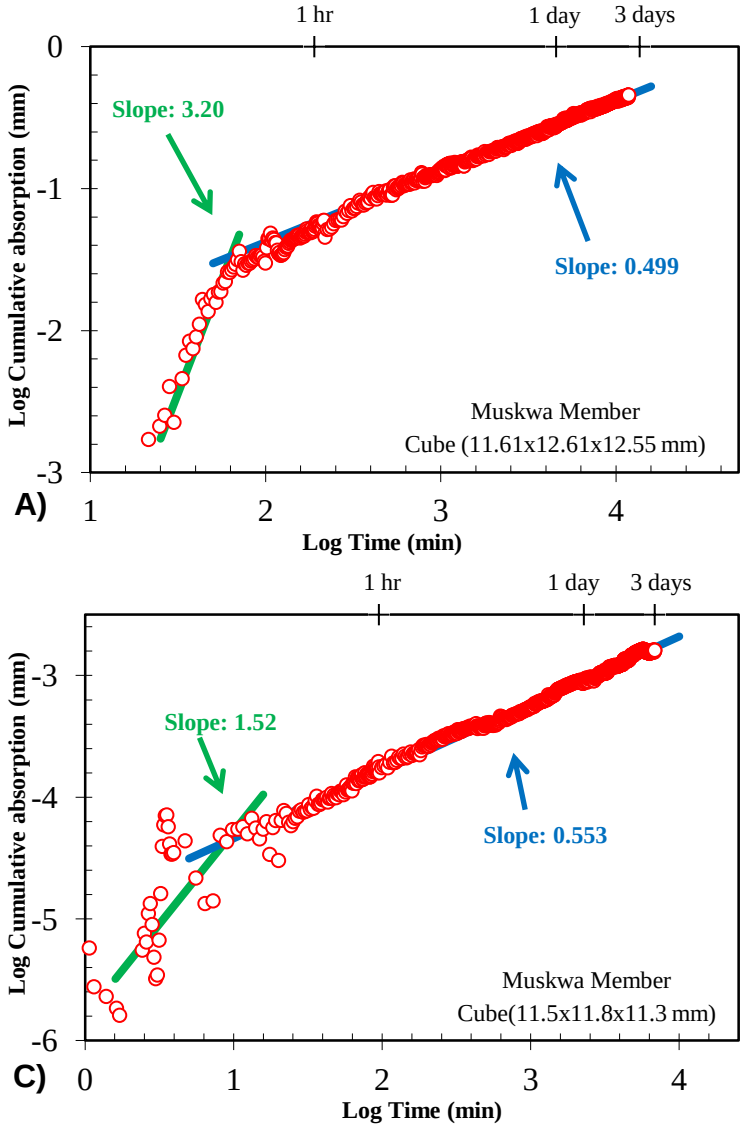

Figure 4-11: Vapor adsorption curves for BC21643MK and BC24577MK. A and C) DI Water, B and D) n-Decane

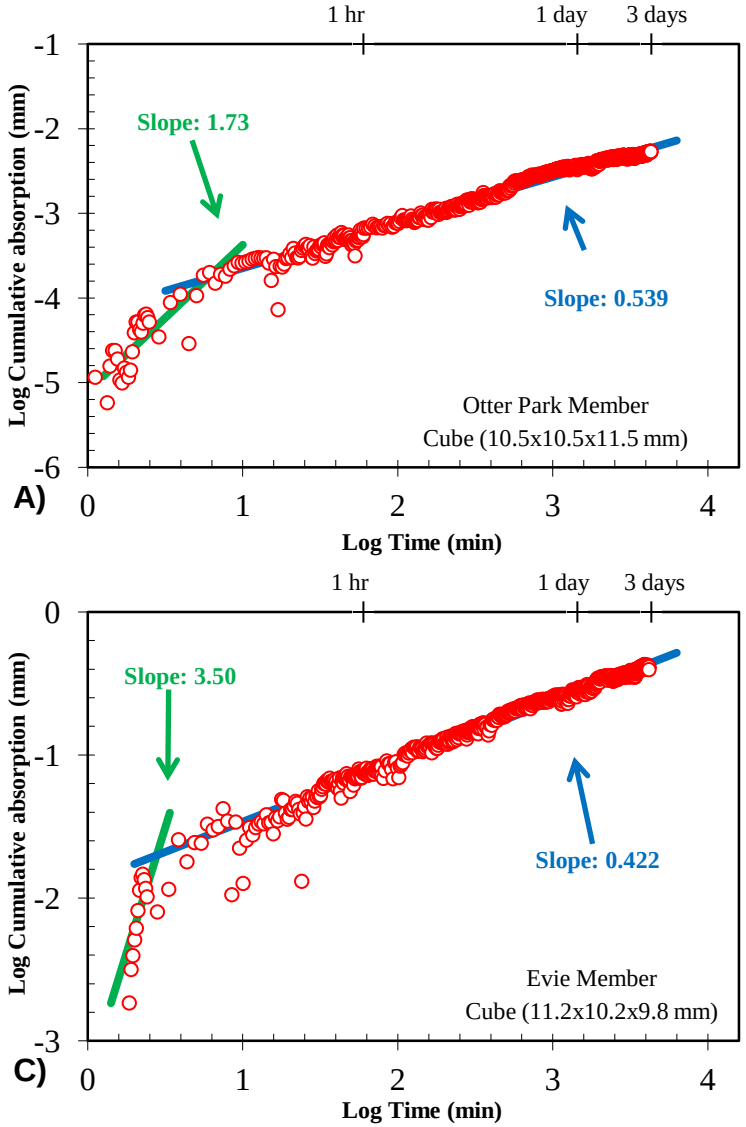

Figure 4-12: Vapor adsorption curves for BC24577OP and BC21643EV. A and C) DI Water, B and D) n-Decane

4-4 Geochemistry and Pyrolysis

Geochemistry

XRD mineralogy data was gathered from Imperial Resources and the BCOGC for both wells and ICP-MS data was gathered for WA# 24577. Whole core XRD is available for WA# 24577, while whole core ICP-MS and only select intervals of XRD results are available for WA# 21643. Whole core data will be used in the analysis and discussion.

The six intervals shown in Figure 4-13 are predominantly composed of quartz and clay with minor concentrations of feldspar, pyrite, dolomite and calcite. The Evie units, which were exposed to detrital carbonate have a respective 13% and 11% calcite concentration. Large sample sets show the Muskwa as quartz rich, the Otter Park as clay rich and the Evie as carbonate rich and these samples reflect that trend well. Sequence stratigraphic work done by Kennedy (2013) has discovered 10 unique lithofacies within the formation. Our plot using Schlumberger's (2014) ternary lithofacies diagram returns 6 lithofacies. The Evie member appears to have 2 distinctly different facies groups. As the Evie formation approaches the underlying Keg River carbonate, massive carbonate facies are seen. Other works have narrowed down lithofacies into fewer categories: massive mudstones, laminated mudstones, bioturbated mudstones and carbonate rich mudstones (Dong, 2015). Chalmers (2012) and Dong (2015) have both investigated not only the characterization of shale pore systems but also the controls, lithologic and others, which create and modify them. We will investigate the correlations between the pore system's morphology and properties to geochemical data in the discussion.

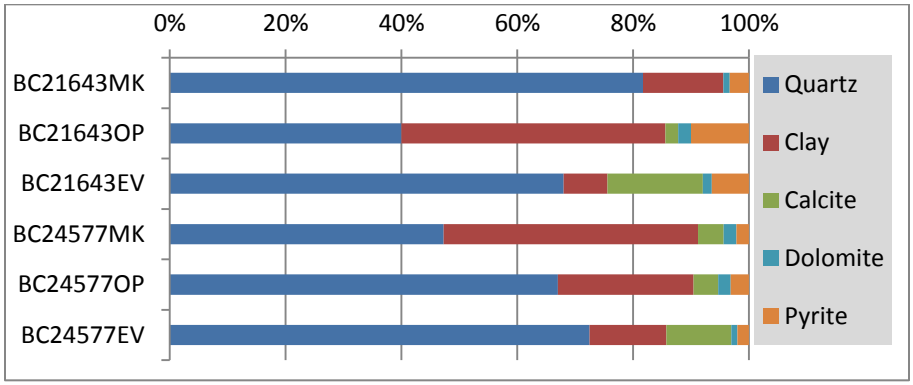

Figure 4-13: XRD Mineralogy for selected project intervals. Both wells.

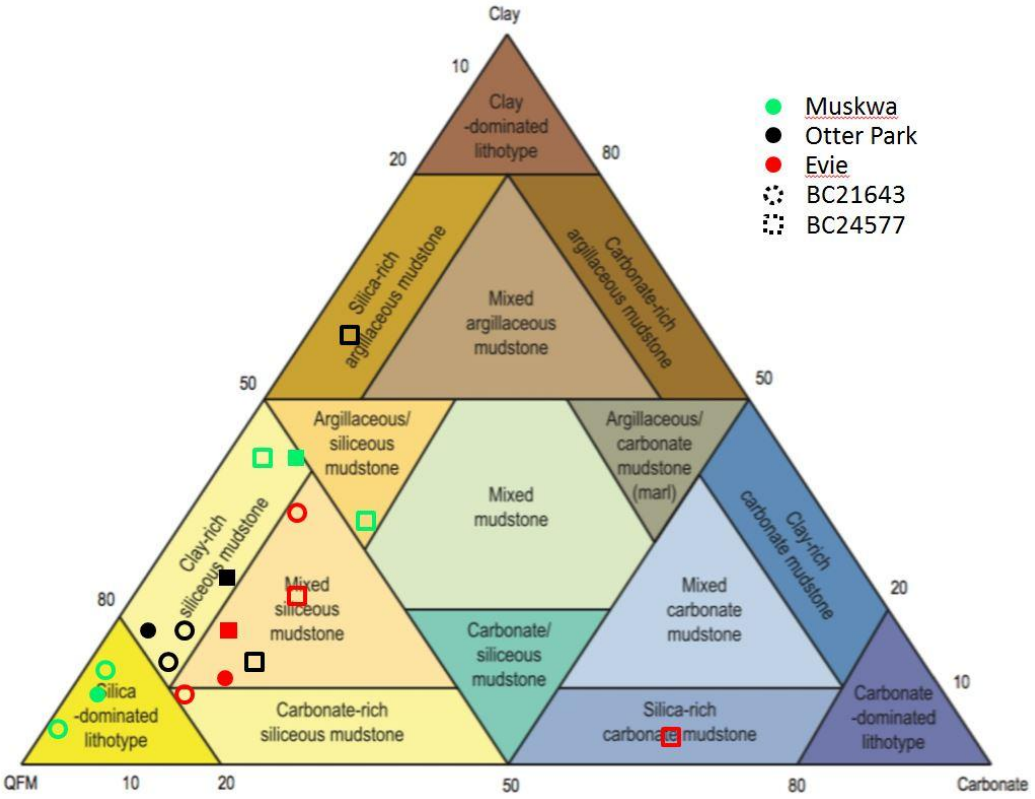

Figure 4-14: Schlumberger (2014) ternary lithfacies plot. Filled shapes are sample intervals and un-filled shapes are extra intervals selected from the dataset.

Pyrolysis

Table 4-5 shows the selected Rock-Eval data from intervals chosen for this study. The full list of whole core pyrolysis data used for data correlation is found in Appendix C. Analyzing hydrocarbon pyrolysis versus TOC has been a standard technique for analyzing the generation potential of hydrocarbons for decades. Langford (1990) and Jarvie (2012) have suggested using primarily S1, the free hydrocarbons available before analysis, and S2, the hydrocarbons produced during the analysis. S3 is a troublesome measurement especially in carbonate rich rocks as the analysis may break down carbon-bearing minerals which will be counted in the measurement (Katz, 1983).

Table 4-5: Pyrolysis data from project select depths

Sample ID	TOC (wt. %)	S1 (mg/g)	S2 (mg/g)	S3 (mg/g)	T Max (°C)
BC21643MK	6.44	0.351	0.169	0.300	322
BC21643OP	4.02	0.280	0.150	0.220	-1*
BC21643EV	3.48	0.528	0.315	0.410	-1*
BC24577MK	2.37	0.770	0.140	0.650	338
BC24577OP	2.58	0.290	0.270	0.240	340
BC24577EV	4.34	1.094	0.730	0.530	356

* Unable to obtain a T Max value for the selected interval

Figures 4-15 and 4-16 show pseudo-van Krevelen diagrams juxtaposed with TOC vs. S2. The van Krevelen diagrams show a kerogen type of III-IV which is consistent with literature values for the region. These wells are over-mature and gas prone, and the S2 values are << than those in successful oil and gas wells (5-10 mg HC/g). Given the significant correlation with S2 there is a causal relationship between the two, but quantitatively they are unappealing prospects. It should be noted that a higher correlation with S2 is possible, but given the clay-rich and extremely impermeable nature of the rocks, it is very likely that hydrocarbons generated during pyrolysis were trapped by adsorption during the process.

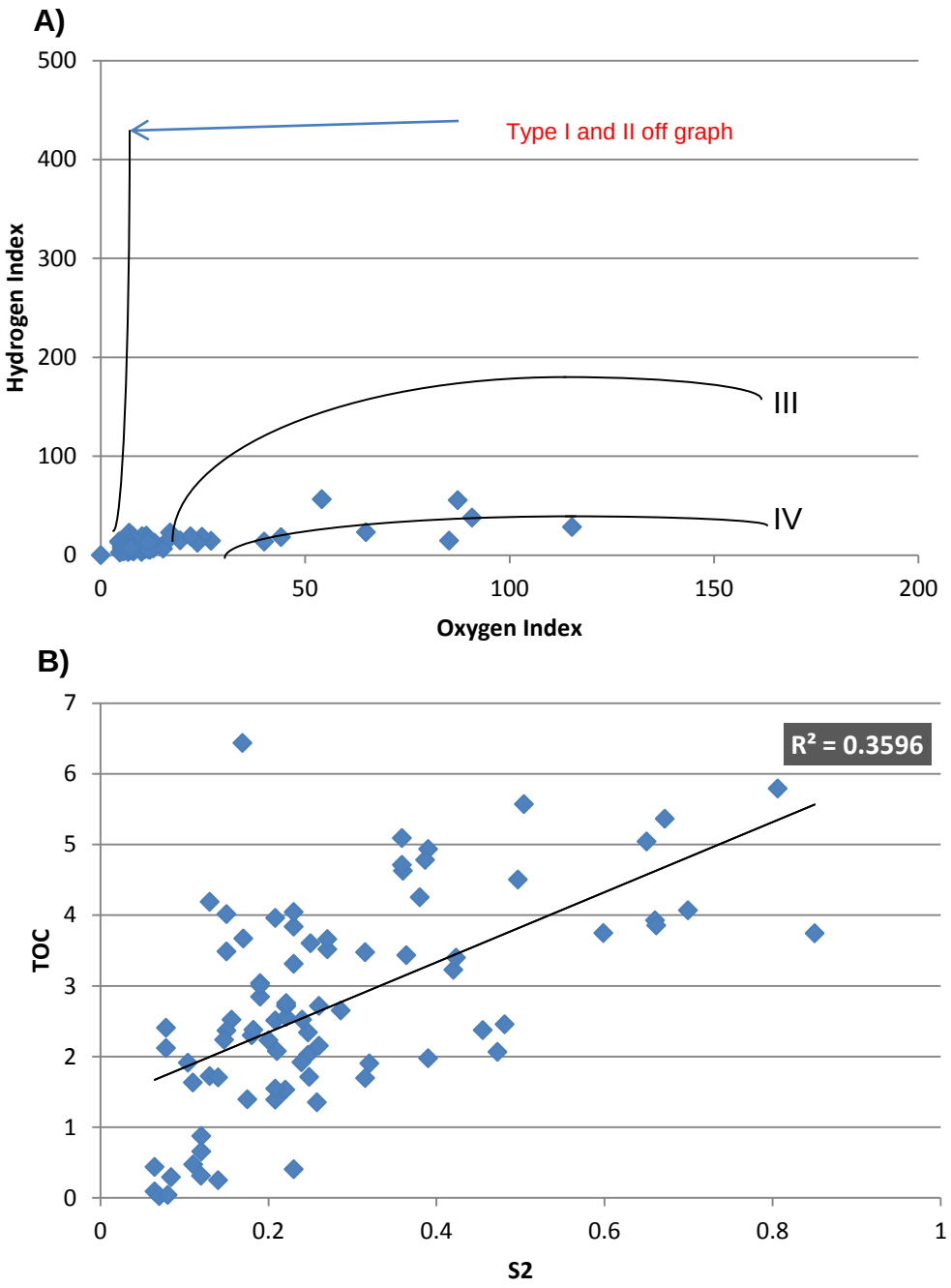

Figure 4-15: A) pseudo-Van Krevelan Diagram and B) TOC/S2 for WA# 21643

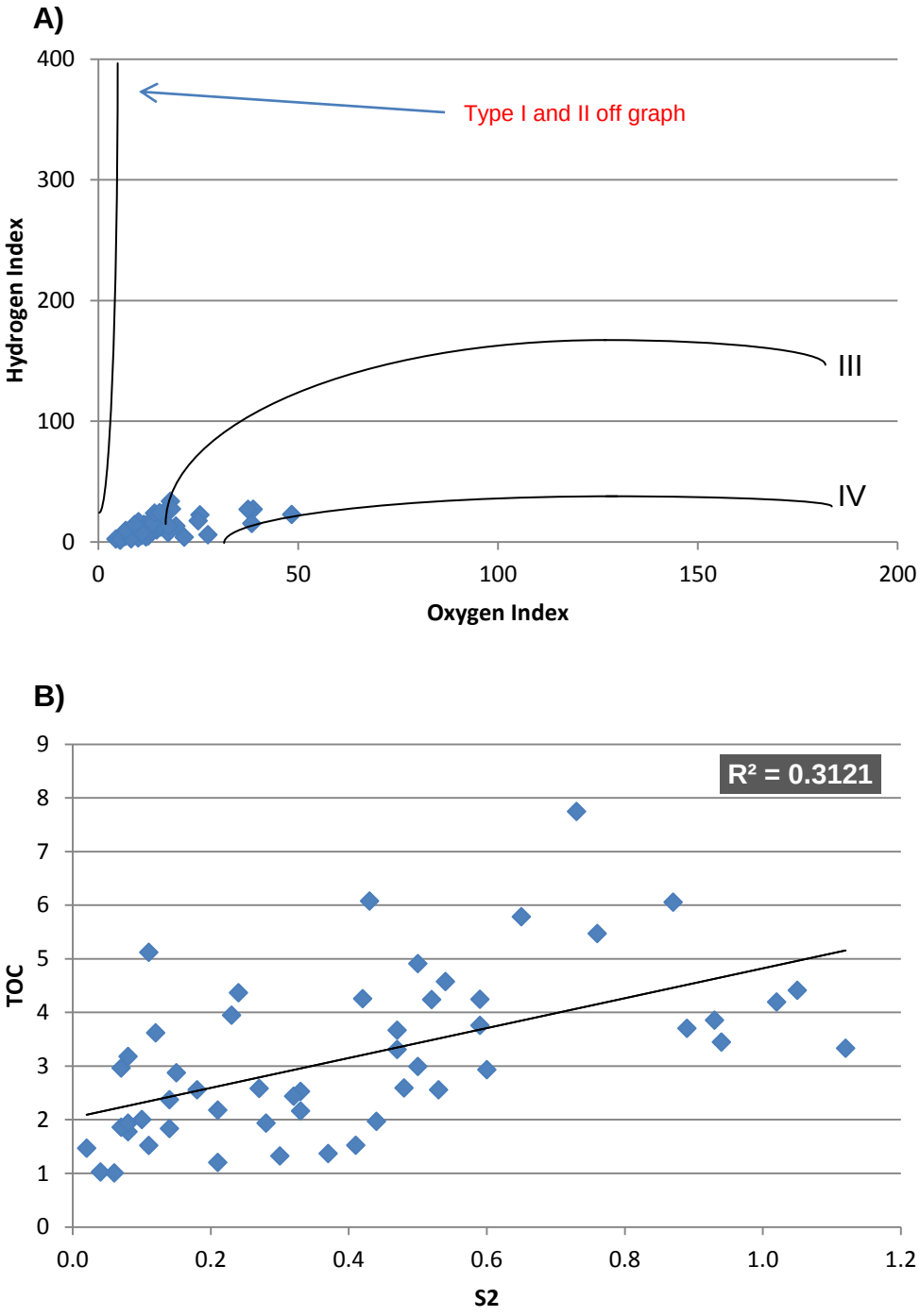

Figure 4-16: A) pseudo-Van Krevelan Diagram and B) TOC/S2 for WA# 24577

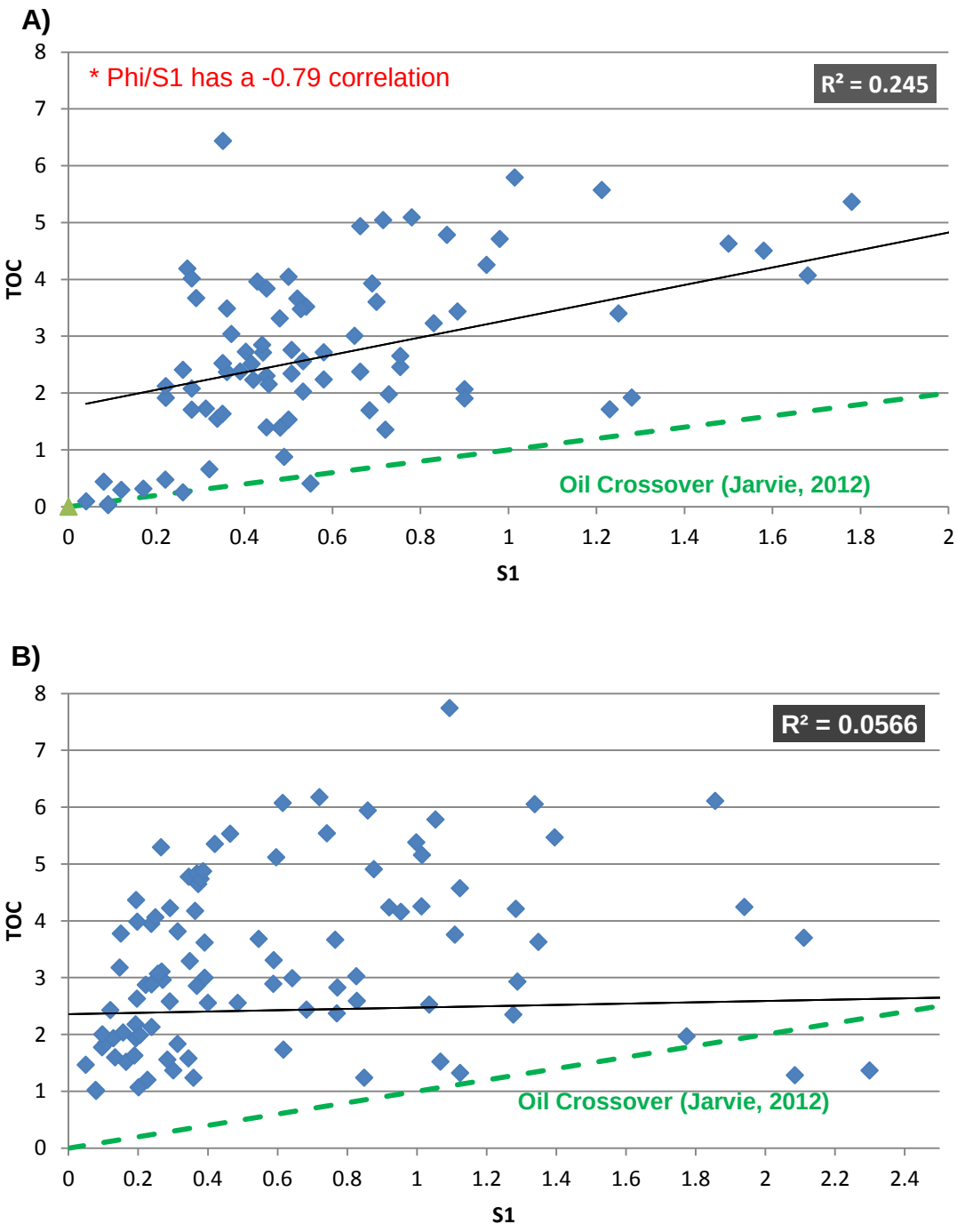

Figure 4-17: TOC vs. S1 for A) WA# 21643 and B) WA# 24577

Figure 4-17 shows plots of TOC vs. S1 with an overlay of the oil crossover line from Jarvie (2012). It is clear that all but approximately 3 points lie above and outside of the oil crossover zone. This tells us that there is either no oil present, or that any oil is trapped within the rock. As stated previously, the Horn River shales are dry gas producing, mature to over mature and type III-IV kerogen. However WA# 21643 shows a 0.245 correlation with S1. Its correlation between porosity and S1 is -0.79, suggesting that the quantitatively small amount of liquid hydrocarbons which were in place resided in organic porosity (Munira, 2015).

Chapter 5

Discussion

Mineralogy, organic geochemistry, pore geometry and topology, and fluid types and phases have all been discussed herein as contributing factors to both hydrocarbon producibility and fluid loss during the drilling and completion process. Furthermore, the micropore networks in oil and gas shales have been shown to be present and therefore develop in a variety of ways. Kuila (2012) has shown that in the Niobrara, nanopores strongly correlate with clay abundance, and Hubbert (2015) has shown that nanopores can also exist primarily in organic matter.

Imbibition and Wetting Characteristics

Figure 5-1 is a graph of imbibed volumes of water plotted against the measured contact angles for the sample along with petrophysical and geochemical values. Although higher contact angles for DI water suggest that water uptake should be less than that of n-Decane, the opposite is true. This has been verified by Lan (2015). Edge accessible organic or organic coated pores may be responsible for the highly oil wetting surface but poorly imbibing nature of n-Decane. Long term imbibition of water is favored over

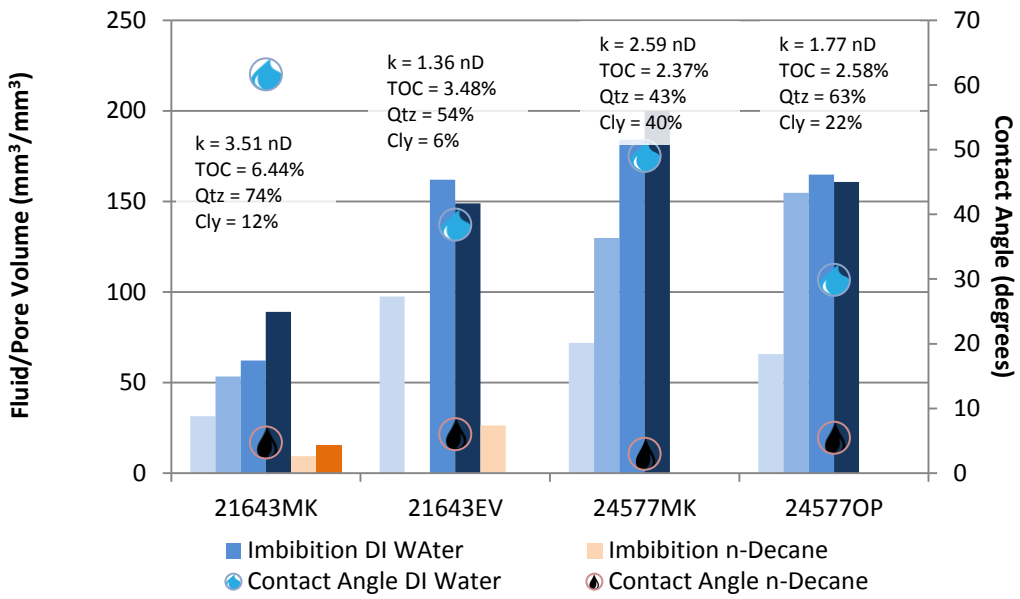

Figure 5-1: Imbibition and Contact Angle Results.

n-Decane by volume and possibly suggests a connected network of hydrophilic pores within the sample. In Figure 5-1, there is a correlation with quartz (%) and DI water contact angle while water imbibition volume appears to be a function of TOC. Water contact angles are higher in samples with more quartz and water imbibition volumes are higher in samples with *lower* TOC. However n-Decane slopes are still around 0.5 which are consistent with a well-connected, oil-wetting pore network. Given the imbibition data gathered, the volumes of n-Decane imbibed are low relative to water imbibed. While MICP data show a predominantly small network of pore throats, the interaction with clay minerals increases water volume imbibed. The correlation of water imbibed vs. clay content is 0.85

Pore and Pore Throat Characteristics

The petrophysical investigation in Chapter 4 revealed that the majority of the throat sizes were in the range of 2.8 – 5 nm. Their deviation in size relative to pore

volume and area, however, was typically very small. Hubbert (2015) and Curtis (2010) have suspected that these small throats of similar size also have similar origins. Thermal

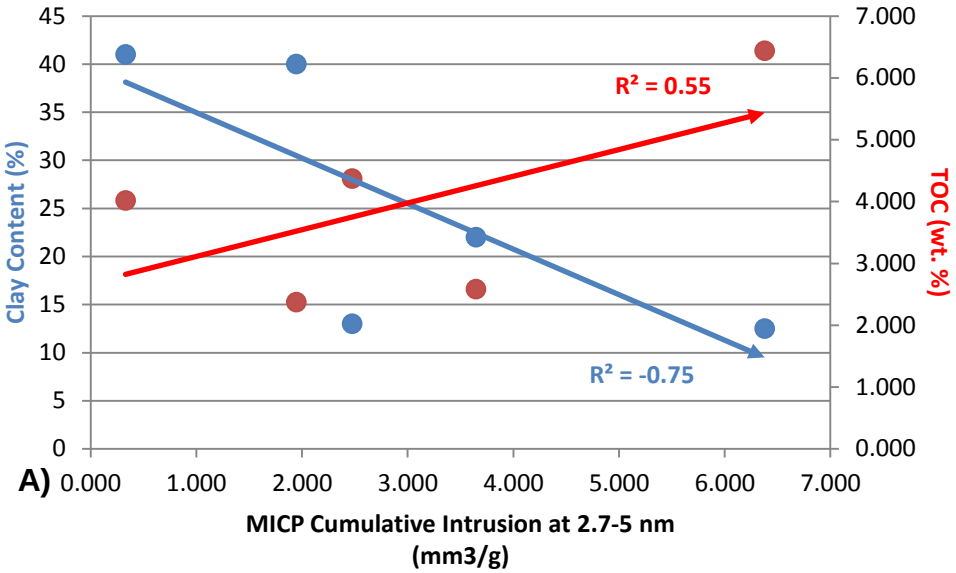

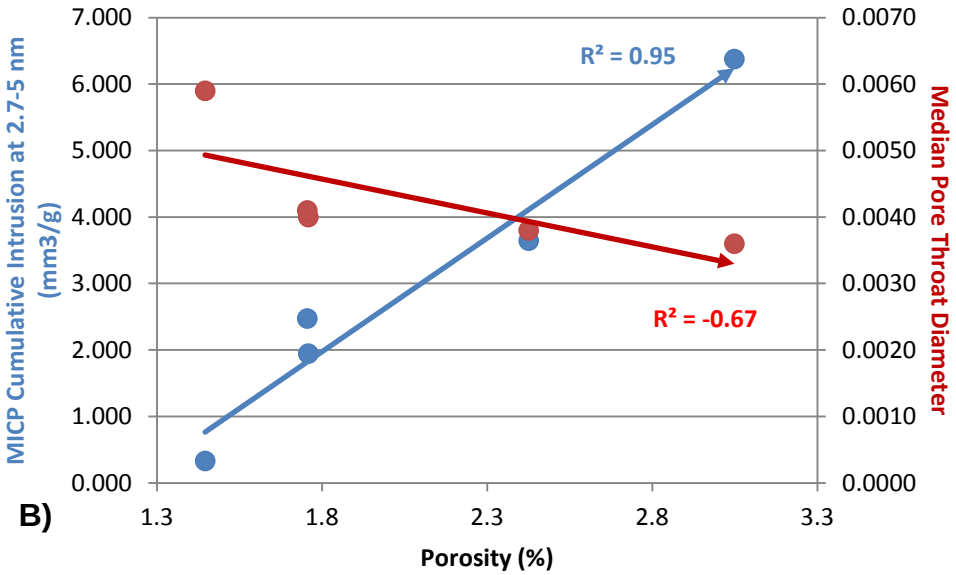

Figure 5-2: A) Clay and TOC relationship with nano-pore intrusion and B) Nano-pore Intrusion and median throat diameter relationship with porosity.

maturity and kerogen diagenesis play a role in creating the throats, primarily micro-fractures, in the Horn River system.

Figure 5.2 reinforces this notion. The throats in the nano range have a 0.55 correlation with TOC and negative 0.75 correlation with clay. In contrast, the Barnett and other shale plays have nearly zero natural fractures present and nano-porosity resides within clays. While it is true that pore throats and micro-pores do not dominate the clays within the Horn River, it may also be true that clay content serves to reduce the amount of small pores and pore throats. In Figure 5-3A, clay content reduces the pore area to volume ratio and reduces the number of small nano-pores making it possible to hold less adsorbed gas on the surface area. The larger pores in contrast may play an important role in transporting gas stored in nano-pores to natural and induced fractures and the well bore. Clay content also inhibits hydraulic fracture propagation and causes significant fluid loss. Previous research has shown this high correlation between small pore throats and TOC and attributed these throats to cracks created during diagenesis which become the primary migration pathways as oil and gas migrate to larger, backbone pores. In Figure 5-2B, the pore throat diameters become smaller in more porous samples while the amount of nano-pores correlates 0.95 with porosity. Figure 5-3B shows mineralogical and porosity relationships with TOC. It is clear here that quartz and porosity both increase with TOC. Chalmers (2012) and Harris (2013) have found that relationship may be due to partially biogenic quartz. No direct relationship was found between mineralogy and permeability. The mineral species in the Horn River have several origins which affect the rock fabric and could in turn influence permeability indirectly.

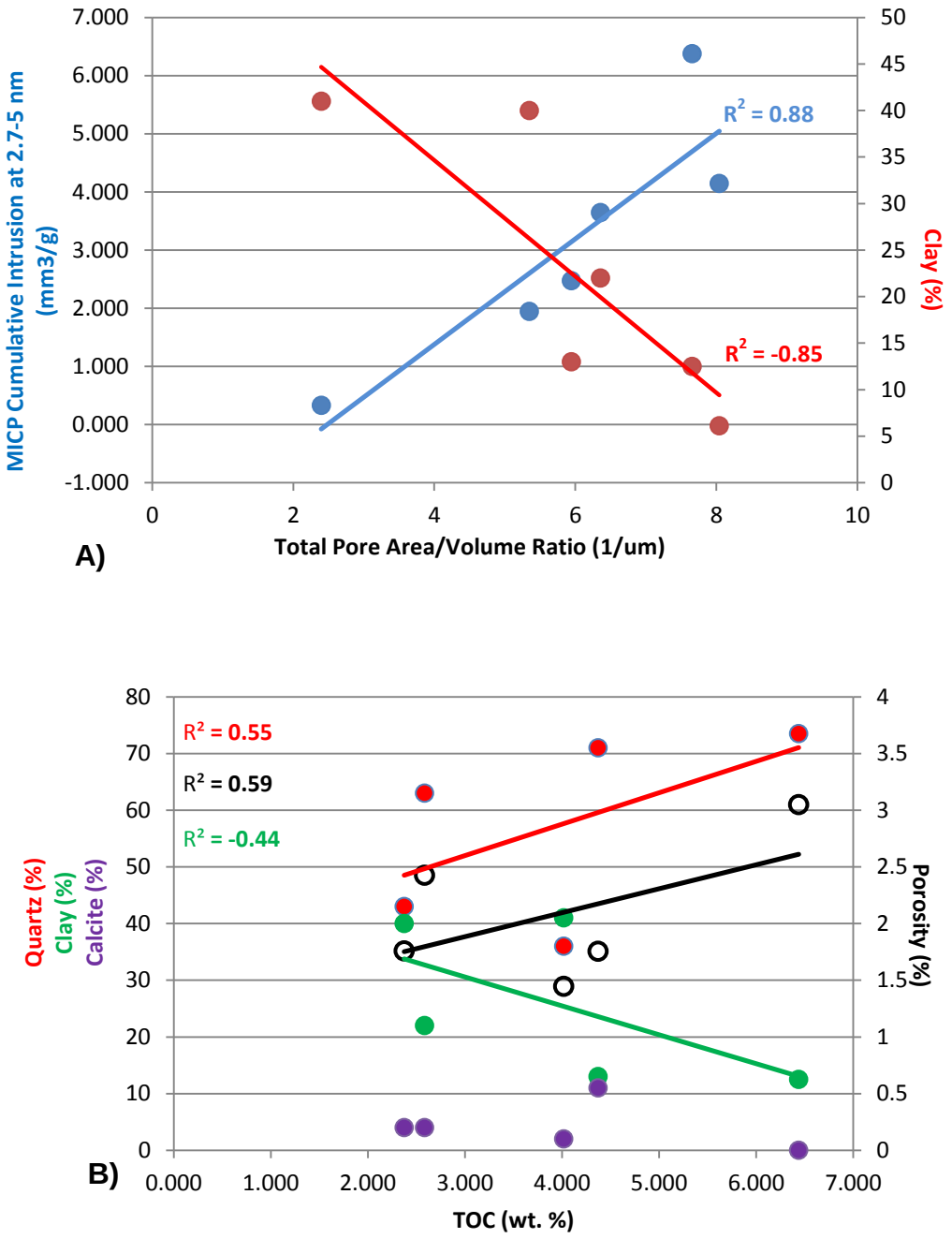

Figure 5-3: A) Micro-porosity and Clay's relationship to Total Pore Area to Volume Ratio. B) Relationship between TOC, Porosity and Mineralogy

Producibility

The inorganic fraction of the material influences pore sizes and distributions while it is the organic fraction within the Horn River that most greatly influences gas storage capacity as organic content (and certain clays) has a large surface area internally (Ross and Bustin, 2008). In contrast to Ross and Bustin (2008), this research found that silica content varies directly with total pore area and clay varies indirectly with it given the samples studied. However the clay fraction still plays an important role in the system. Bringing in gas-filled porosity for well BC24577 (Appendix C) in Figure 5-4, there appears to be an optimal clay fraction at ~20% at which gas filled porosity and TOC are at their highest. It appears given the previously discussed figures that too little clay may raise the micro-pore space while too much clay inhibits the gas storage potential. Pore area is necessary as most gas in a dry gas, high pressure system is adsorbed. Clay (%) vs. water volume imbibed correlates at 0.85.

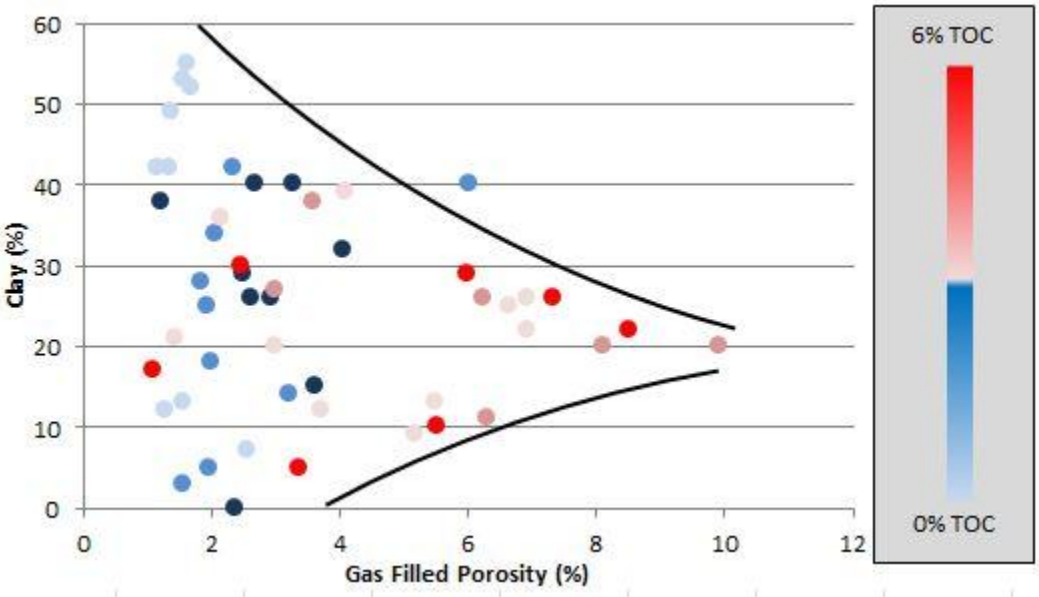

Figure 5-4: Clay (%) vs. gas filled porosity for well BC24577. An optimal clay concentration of approximately 20% is seen with the highest TOC concentrations.

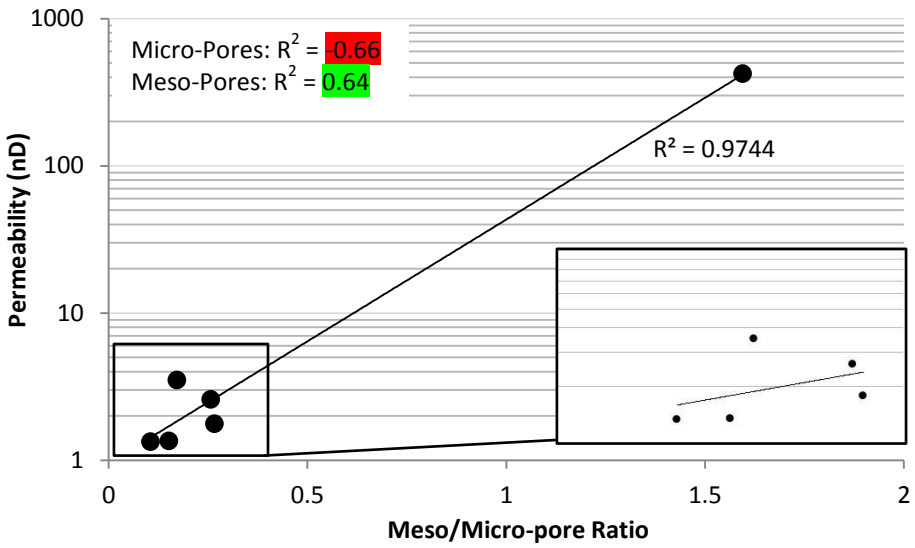

Figure 5-5: Permeability vs. Meso-Micro-pore ratio

Permeability, while not directly influenced by mineralogy as mentioned earlier and verified by Chalmers (2012), is however influenced heavily by the distribution of pore and pore throat apertures. Sustained flow rates in shales require large pore networks of a combination of intergranular, natural and induced fractures to connect micro-porosity with the well bore. They also require micro-pores as they are the primary place for gas storage in many of these types of reservoirs. In Figure 5-5, permeability is compared with meso- and micro-pores and their ratio. While Micro-pores exhibit a negative correlation with permeability and meso-pores exhibit an equally strong positive correlation, their ratio has a correlation coefficient of 0.97. It is clear that permeability in shale reservoirs is a function of a combined ratio of a large and small pore system.

Petrophysical data for these wells did not return any relevant controls on pyrolysis, however the sample mineralogy did. Clay content served to reduce the hydrogen and oxygen index. It is likely that any pyrolyzed hydrocarbons and CO_2 were preferentially trapped within these samples and not analyzed while samples rich in quartz

allowed the gases to be read by the sensors. Clay-rich zones are also contain less gas to begin with.

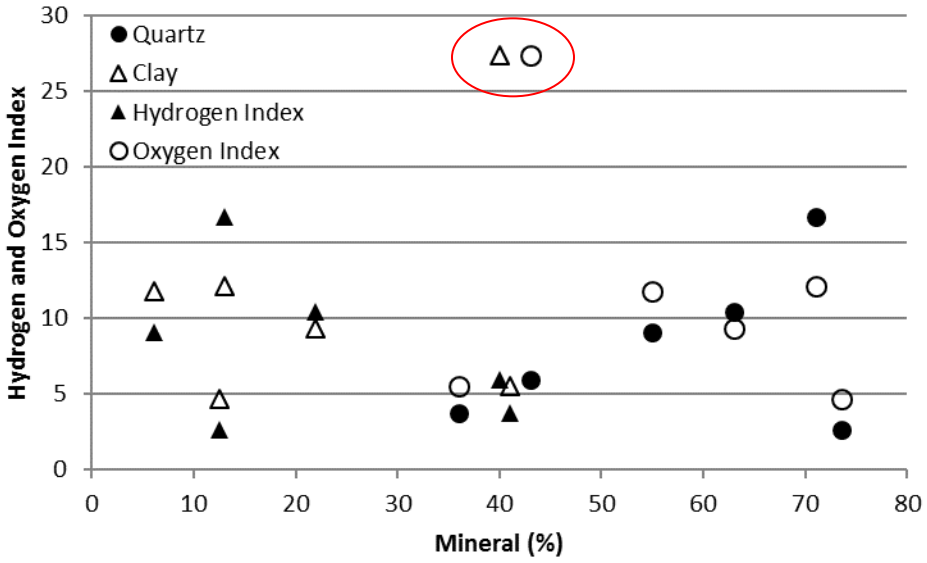

Figure 5-6: Hydrogen and Oxygen index compared with Quartz and Clay content.

Well Log Analysis

The well log models resemble the behavior found in the core studies. Well # 24577 starkly shows the inverse relationship between clay content and porosity also found in core. WA#21643, with a lower overall clay content shows this subdued trend as well. Core and log porosities qualitatively trend together, however there a few instances where GRI porosity is higher than the PHIE log and MICP porosity lower. In a few cases this is likely due to core depths inaccurately scaled to log depths, but elsewhere there are discrepancies that must be explained. At 2250 m on WA# 24577, GRI porosity is 7.5-10 while log porosity is less than 5. Estimating porosity in carbonates requires a sonic log as

density and neutron logs do not detect secondary porosity in this facies. The presence of carbonate at this interval reduces the log porosity reading.

TOC core and log results are in agreement. There are cases, however, where log TOC is higher than core TOC. This occurs in clay rich zones primarily. In WA #24577 from 2255 – 2275m and from 2330 – 2360 m, the resistivity profile is augmented and TOC appears higher than core TOC. Core TOC is higher in carbonate rich zones. Clay/TOC core correlations match the well logs model. High clay zones typically have low TOC. In determining net pay intervals, the core studies were considered and used to create cut-off values. The net pay inputs used were: TOC > 2.5, 17% < Clay < 23%, and Deep Resistivity > 20 Ohmm. Given that these two wells are wildcat and experimental vertical wells, pay was found to be very low, approximately 36 feet in only 1 well. Pay is delineated by the green bar in the depth track on Figure 5-7.

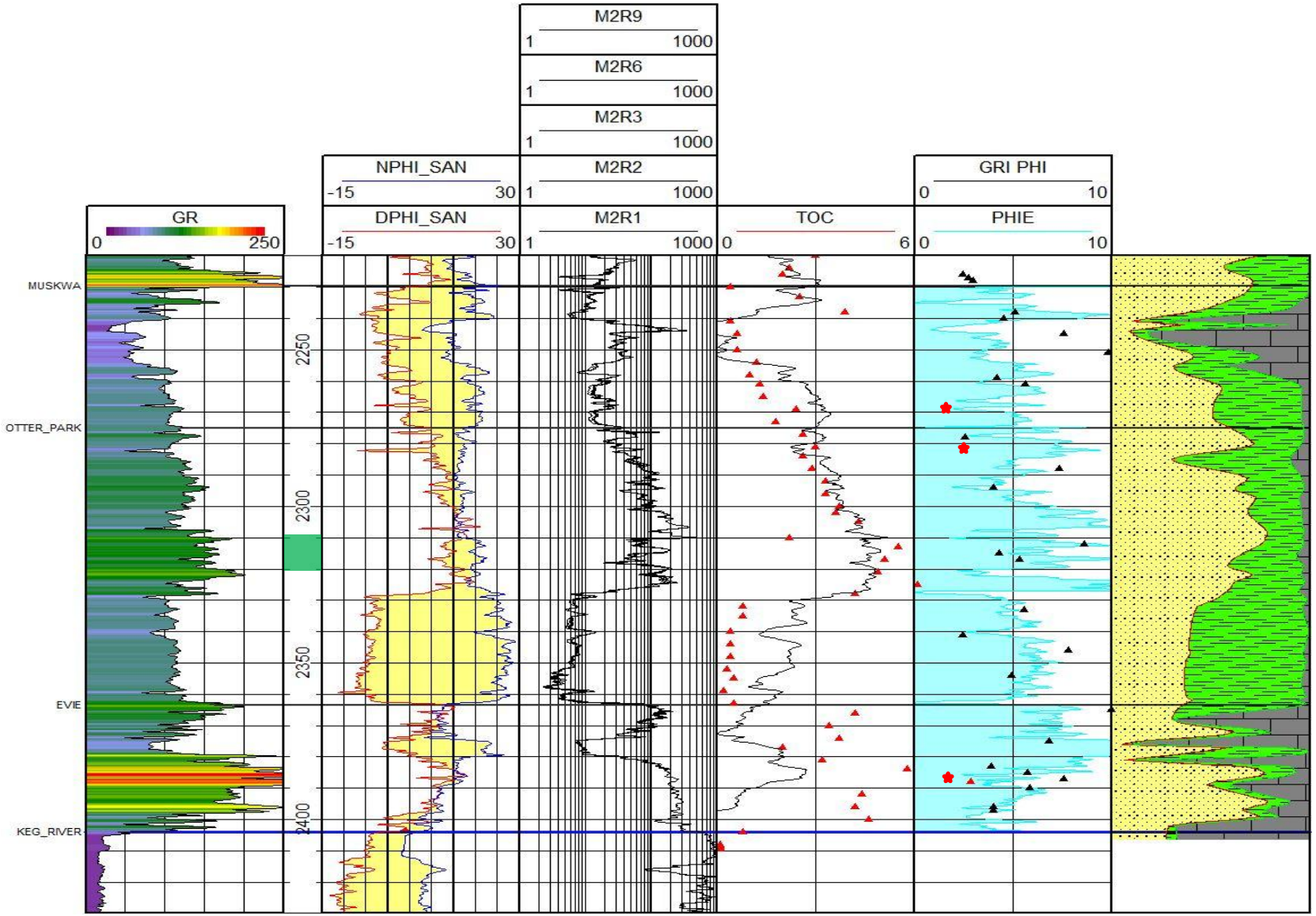

Figure 5-7: Well log model of WA# 24577. Red stars in the porosity track are MICP porosity values. The green bar in the depth track shows the potential pay interval.

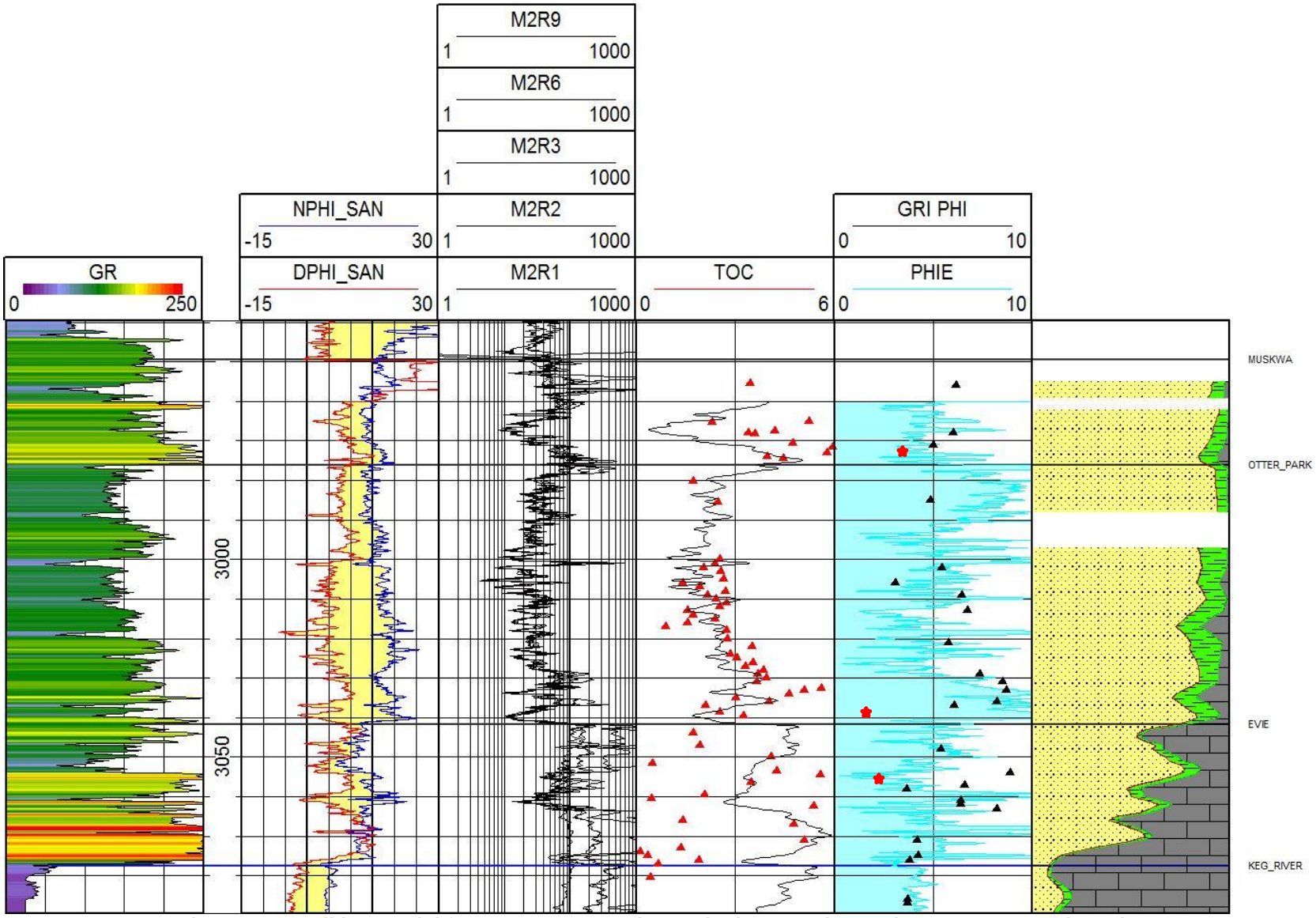

Figure 5-8: Well log model for WA# 21643. Red stars is the porosity track are MICP porosity values.

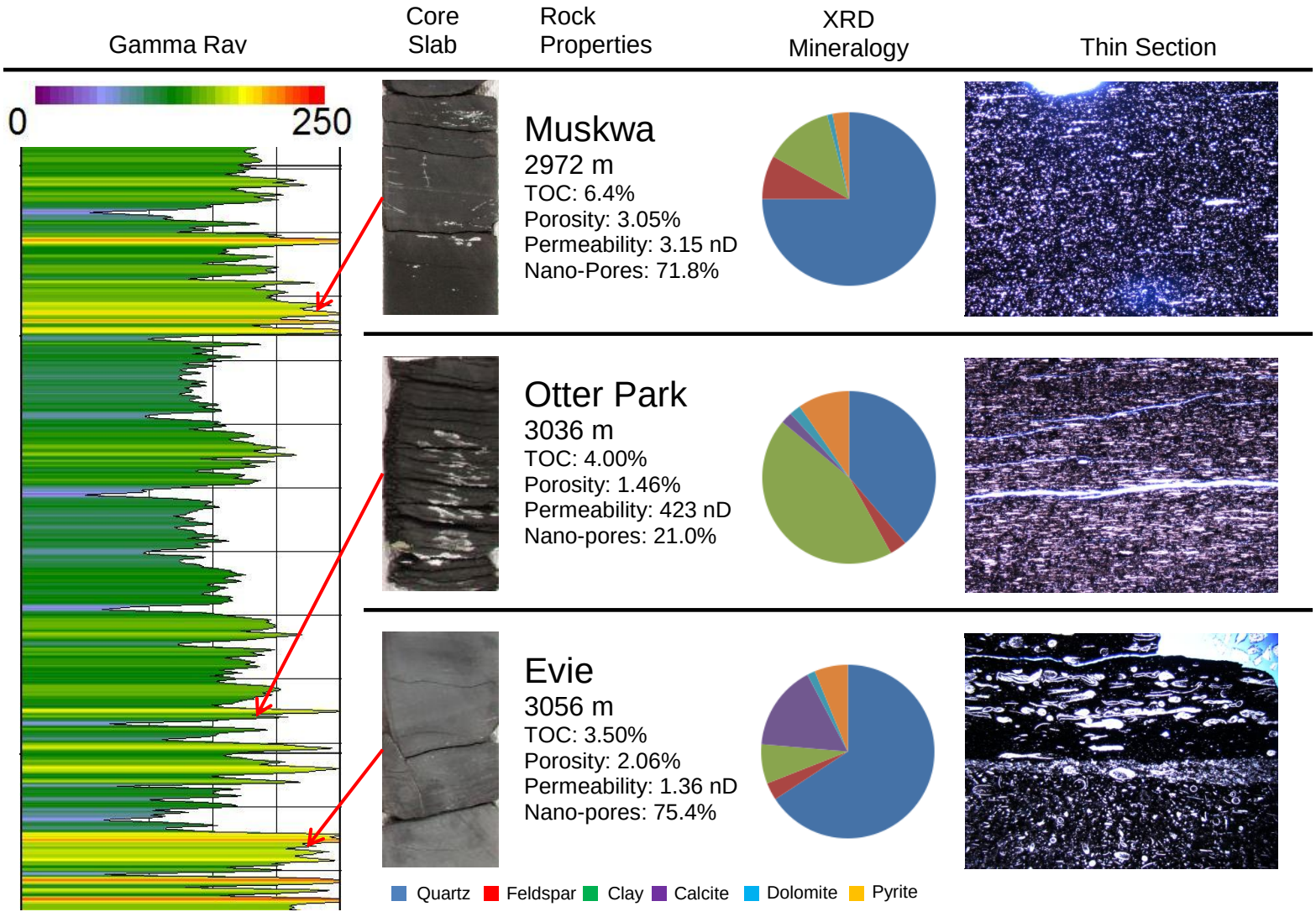

Figure 5-9: Multi-scale from well log to thin section displaying rock properties at each scale.

Conclusions

This study combined several sources of data to study the geochemical and petrophysical controls on producibility in the Horn River shales. The Muskwa, Otter Park and Evie members are generally clay rich, siliceous mudstones, but the Evie member contains a carbonate rich facies as well. Quartz and clay are the primary mineral controls in the system. Through contact angle measurements and imbibition experiments conducted with DI water and n-Decane, the samples were found to have two distinct sets of pore networks, a hydrophilic network able to imbibe large volumes of water and a less connected hydrophobic network which imbibes n-Decane but comprises a smaller amount of the porosity by volume which exists. Imbibed water volume varies directly with clay and indirectly with TOC in support of this. The majority of pores in the samples exist in the range of 2.8 – 5 nm and these have a high degree of correlation with both porosity and TOC and are likely genetically related. This suggests that the nano-pores in the Horn River developed as a network of micro-fractures which are the bi-product of diagenesis and kerogen cracking. Pyrolysis data indicate, however, that the Hydrogen Index decreases as porosity – micro-porosity – increases. The organic pores present do not readily release pyrolyzed hydrocarbons. Permeability shows a strong relationship not simply with porosity which is mineralogically controlled, but with the ratio of macro- to micro-pores. It is necessary to have a high fraction of large pores to allow transport to the well bore and a high enough fraction of small pores to store economic quantities of gas. A clay content of approximately 20% produces optimally high values of TOC while concentrations of clay which deviate significantly higher or low reduce the gas-filled porosity and TOC.

Tying core data to log data produced a well log model consistent with core data and the findings made. Core and log generated porosity and TOC increase together. In general, the high amount of CH_3 and kerogen within the system cause the porosity logs to read high and overestimate the effective porosity in the system. While both of the wells used in this project were non-producing, experimental wells, zones near 20% clay with high TOC would be an optimal zone for production as a large and small pore network is highly potential there. These cutoffs produced about 35 feet of pay in one well.

Recommendations

Lab scale petrophysical analysis is tedious and difficult to translate into a workable, large-scale model. However, identifying region- and reservoir-specific controls with a sample set large enough to produce confidence should be the focus when conducting evaluations such as these. Within the Horn River, organic matter tends to control the creation of a micro-porous network which contains dry gas, but also creates a pore architecture which may be difficult to sustain production. More research into the transport mechanisms within the Horn River, diffusion, advection, capillary action, etc.., is necessary to increase producibility in the formation.

Appendix A

Methods and Procedures for Geochemical Analysis at Weatherford Laboratories

Rock Sample Preparation

Samples for Total Organic Carbon (TOC) and/or Programmed Pyrolysis may each require varying levels of sample preparation. Groups of samples are evaluated as to their respective condition as received and are handled differently depending on the various types of contaminants, lithologies, and analytical objectives. Samples are not high-graded prior to grinding unless specifically instructed by the client. When necessary and as instructed, water washing may be required to remove water-based mud. Solvent washing can be utilized to remove oil-based and/or synthetic-based mud. Additional solvent extraction of the crushed rock will be necessary to completely remove the contaminating oil-based and/or synthetic-based mud. Sample picking may also be necessary to remove lost circulation material or known cavings. Samples for TOC and Programed Pyrolysis are then ground to pass through a fine mesh sieve prior to analysis.

Total Organic Carbon

Approximately 0.10 g of crushed rock is accurately weighed and then digested with concentrated hydrochloric acid to remove all carbonates form the sample. At this point, gravimetric carbonate content can be determined if requested. Following digestion, the sample is washed through a filtering apparatus, placed in a combustion crucible and dried. After drying, the sample is analyzed with a LECO Carbon Analyzer with detection limits to 0.01 weight percent. Standards and sample duplicates are tested regularly to assure superior instrument performance.

Programmed Pyrolysis (Rock-Eval II, Rock-Eval VI, Source Rock Analyzer)

Programmed pyrolysis (Rock-Eval and SRA) is performed to assess source rock quality and thermal maturity (e.g., Peters, 1986; Peters and Casa, 1994). In programmed pyrolysis, crushed rock samples are heated in an inert environment to determine the yield of hydrocarbons and CO2. The sample is initially held isothermally at 300°C for 3 minutes, producing the S1 peak by vaporizing the free (unbound) hydrocarbons. High S1 values indicate either large amounts of kerogen-derived bitumen (as in an active source rock) or the presence of migrated hydrocarbons. The oven then increases in temperature by 25°C/minute to a final temperature of approximately 600°C, depending on the instrument type. During this time, hydrocarbons that evolve from the sample as a function of the pyrolytic degradation of the kerogen are measured, generating the S2 peak and is proportional to the amount of hydrogen-rich kerogen in the rock. The temperature at which the S2 peak reaches a maximum, "Tmax", is a measure of the source rock maturity. Accuracy of Tmax is 1-3°C, depending on the instrument, program rate and sample size, but can also vary by organic matter type. Tmax values for samples with S2 peaks less than 0.2 mg HC/g rock are often inaccurate and should be rejected unless a definitive kerogen peak is noted from the pyrogram. Any carbon dioxide released between 300° and 390°C is also measured, generating the S3 peak, providing an assessment of the oxygen content of the rock. In addition to the standard programmed pyrolysis method, we have several additional methods available designed to provide the client with additional useful information as it relates to the geochemical nature and potential of a rock sample including but not limited to TOC quantification, Carbonate quantification, Reservoir Oil Quality, APIR and Kerogen Kinetic analyses. A summary of analytical results from Programmed Pyrolysis follows.

Results

S1: free oil content (mg hydrocarbons per gram of rock)

S2: remaining hydrocarbon potential (mg hydrocarbons per gram of rock)

S3: organic carbon dioxide (mg CO2 per gram of rock)

TOC: total organic carbon content (wt. %)

Tmax: temperature at maximum evolution of S2 hydrocarbons

Ratios: hydrogen index (HI), oxygen index (OI), production index (PI), S2/S3, and S1/TOC

Appendix B

Methods and Procedures for Geochemical Analysis at TerraTek Laboratories

TRA Geochemistry

LECO Organic Carbon and Rock-Eval II Pyrolysis

Total Organic Carbon is best determined by direct combustion. Approximately 0.15 grams of sample are carefully weighed, treated with concentrated HCl to remove carbonates, and vacuum filtered on glass fiber paper. The residue and paper are placed in a ceramic crucible, dried, and combusted with pure oxygen in a LECO EC-12 or LECO CS-444 carbon analyzer at about 1,000*C. A laboratory standard is run every five samples.

Rock-Eval II pyrolysis is used to determine kerogen type, kerogen maturity and the amount of free hydrocarbons. About 0.1 grams of the same ground sample used for LECO TOC are carefully weighed in a pyrolysis crucible and then heated to 300*C to determine the amount of free hydrocarbons, S1, that is thermally distilled. Next, the amount of pyrolyzable hydrocarbons, S2, is measured when the sample is heated in an inert environment which rises from 300* to 550*C at a heating rate of 25*C/minute. S1 and S2 are reported in mg HC/g sample. Tmax, a maturity indicator, is the temperature of maximum S2 generation. When S2 values are less than 0.2 mg HC/g sample, the S2 maximum typically has poor definition and thus, Tmax cannot be reliably determined (Peters, 1986). Tmax values are reported as N.A. on sampled with 0.00 S2. Carbon dioxide generated during the S2 pyrolysis, an indicator of kerogen oxidation, is collected up to a temperature of 390*C and reported as S3 in units of mg CO_2/g sample. A laboratory standard is run every 10 samples. Hydrogen Index (HI = S2*100/TOC) and Oxygen Index (OI = S3*100/TOC) are used as kerogen type indicators when plotted on a van Krevelen type diagram.

Appendix C

List of Whole Core Pyrolysis, TOC and Gas-filled Porosity Data

21643

Depth (m)	Leco TOC	S1	S2	S3	Tmax (°C)
2955.5	3.44	0.88	0.36	0.29	-1
2965	5.24	0.60	0.21	0.31	-1
2965.2	2.30	0.45	0.18	0.22	304
2967.5	4.19	0.27	0.13	0.28	-1
2968	3.39				
2968.3	3.60	0.70	0.25	0.24	-1
2969.98	5.04	0.72	0.65	0.23	347
2970.5	4.73				
2970.94	4.94	0.66	0.39	0.29	308
2971.5	5.96				
2971.91	6.44	0.35	0.17	0.30	-1
2972.45	5.67				
2972.9	5.79	1.01	0.81	0.26	322
2973.53	4.10				
2973.9	3.96	0.43	0.21	0.31	306
2974.4	4.46				
2978.16	2.34	0.51	0.25	0.22	-1
2980.1	1.73	0.31	0.13	0.19	-1
2980.6	2.70				
2982.2	1.98	0.73	0.39	0.22	312
2982.57	2.13				
2985.61	2.46	0.75	0.48	0.19	324
3000	2.51	0.42	0.21	0.23	-1
3000.4	2.48				
3001	2.38	0.39	0.18	0.23	311
3001.5	1.88				
3002	2.03	0.53	0.25	0.22	-1
3002.49	1.79				
3003	2.56	0.53	0.22	0.17	304
3003.5	1.91				
3004.1	2.38	0.66	0.46	0.24	308
3004.5	1.51				
3005	2.65	0.75	0.29	0.18	303
3005.49	2.65				
3006	1.39	0.48	0.21	0.27	-1
3006.5	2.40				
3007	1.91	0.22	0.10	0.23	-1
3007.33	2.43				
3008	2.71	0.44	0.22	0.23	-1
3008.5	2.32				
3009	2.15	0.46	0.26	0.18	-1
3009.6	2.22				
3010	2.41	0.26	0.08	0.24	302
3010.5	2.85				
3011	2.73	0.40	0.22	0.26	-1
3011.5	2.32				
3012	2.52	0.35	0.16	0.27	-1
3012.5	2.38				
3013	1.53	0.50	0.22	0.16	314
3013.5	1.66				

3014.02	1.71	0.28	0.14	0.18	-1
3014.5	2.05				
3015	2.37	0.36	0.15	0.16	-1
3015.5	2.85				
3016	1.55	0.34	0.21	0.16	407
3016.5	0.71				
3017.03	0.88	0.49	0.12	0.35	-1
3017.5	2.88				
3018	2.72	0.58	0.26	0.17	-1
3018.4	2.42				
3019.1	2.23	0.42	0.20	0.16	-1
3019.5	2.74				
3020	2.76	0.51	0.22	0.19	-1
3020.53	2.94				
3021.1	2.12	0.22	0.08	0.17	-1
3021.5	2.93				
3022	3.49	0.36	0.15	0.20	319
3022.5	1.40				
3022.9	1.63	0.35	0.11	0.21	485
3023.5	1.99				
3024	2.85	0.44	0.19	0.15	-1
3024.5	3.09				
3025	3.04	0.37	0.19	0.19	-1
3025.5	3.15				
3026	3.52	0.54	0.27	0.18	302
3026.5	3.12				
3027	3.31	0.48	0.23	0.26	-1
3027.5	3.37				
3028	3.84	0.45	0.23	0.20	-1
3028.5	2.91				
3029	3.67	0.29	0.17	0.28	-1
3030	3.93	0.69	0.66	0.24	353
3030.6	4.03				
3031	3.66	0.52	0.27	0.21	-1
3032	4.89				
3032.5	5.61	0.58	0.34	0.29	-1
3033	4.91				
3033	5.09	0.49	0.27	0.27	-1
3033.5	5.57				
3034	4.63	1.50	0.36	0.27	-1
3034.5	3.52				
3035	3.01	0.65	0.19	0.33	-1
3035.5	2.56				
3036	4.02	0.28	0.15	0.22	-1
3036.5	3.60				
3037	2.08	0.28	0.21	0.21	-1
3037.48	2.23				
3038.5	2.52	0.35	0.24	0.17	-1
3039.2	3.34				
3039.5	3.23	0.83	0.42	0.26	560
3041.2	3.75	2.19	0.85	0.26	353
3044	1.71	1.23	0.25	0.46	-1
3044.37	0.95				
3047	1.92	1.28	0.24	0.25	-1
3047.48	1.91				

3048.1	2.24	0.58	0.15	0.34	-1
3050	4.07	1.68	0.70	0.29	305
3050.4	1.79				
3051.56	0.48	0.22	0.11	0.31	340
3051.9	3.80				
3052.4	3.86	2.28	0.66	0.27	-1
3053	3.69				
3053.5	4.26	0.95	0.38	0.22	-1
3053.9	5.87				
3054.5	5.57	1.21	0.50	0.31	307
3055	5.57				
3055.37	3.75	2.06	0.60	0.30	-1
3056	3.54				
3056.5	3.48	0.53	0.32	0.41	-1
3057	3.25				
3057.45	0.30	0.12	0.08	0.34	310
3058	2.86				
3058.4	1.70	0.68	0.32	0.42	-1
3059	2.89				
3059.5	2.07	0.90	0.47	0.35	-1
3059.91	3.47				
3060.5	0.44	0.08	0.06	0.37	488
3061	4.00				
3061.49	4.51	1.58	0.50	0.28	-1
3061.9	1.37				
3062.5	5.37	1.78	0.67	0.39	-1
3063.4	4.71	0.98	0.36	0.39	-1
3064	5.15				
3066	1.40	0.45	0.17	0.33	-1
3067	4.78	0.86	0.39	0.32	-1
3069.31	4.05	0.50	0.23	0.47	-1
3071	5.09	0.78	0.36	0.37	-1
3071.5	3.68				
3072.1	3.40	1.25	0.42	0.40	-1
3072.5	3.51				
3073.05	1.35	0.72	0.26	0.30	304
3073.5	1.46				
3074	0.09	0.04	0.06	0.26	467
3074.5	0.40				
3075	0.32	0.17	0.12	0.29	360
3076	1.90	0.90	0.32	0.32	-1
3077	0.66	0.32	0.12	0.29	-1
3077.98	1.10	0.45	0.13	0.31	-1
3079.52	1.39				
3080.5	0.41	0.55	0.23	0.22	354
3081.54	0.09				
3082.97	0.03	0.09	0.07	0.21	512
3084.44	0.03				
3085.95	0.04	0.09	0.08	0.22	509
3088	0.21				
3090	0.25	0.26	0.14	0.22	367

24577

Depth (m)	Leco TOC	S1	S2	S3	Tmax (°C)
2181.79	0.344				
2183.60	0.579				
2190.74	1.519	0.165	0.110	0.140	
2194.02	1.007	0.079	0.060	0.110	
2198.00	1.467	0.049	0.020	0.080	301.000
2201.28	1.775	0.096	0.080	0.120	347.000
2204.57	1.858	0.108	0.070	0.110	390.000
2207.00	1.935	0.193	0.280	0.220	340.000
2210.30	1.934	0.129	0.080	0.230	319.000
2213.60	2.556	0.486	0.530	0.410	345.000
2216.98	2.874	0.222	0.150	0.310	338.000
2220.30	2.962	0.270	0.070	0.130	
2223.58	2.178	0.193	0.210	0.170	311.000
2226.45	1.968	1.774	0.440	0.500	342.000
2229.73	0.444				
2233.01	2.526	1.035	0.330	0.490	324.000
2237.55	3.947	0.237	0.230	0.270	-1.000
2241.33	0.428				
2245.16	0.564				
2250.10	0.644				
2253.90	1.202	0.226	0.210	0.300	314.000
2257.55	1.024	0.078	0.040	0.220	320.000
2261.34	1.323	1.124	0.300	0.640	337.000
2265.32	1.368	0.301	0.370	0.530	511.000
2269.12	2.372	0.770	0.140	0.650	338.000
2273.13	1.834	0.313	0.140	0.320	
2276.93	2.582	0.290	0.270	0.240	340.000
2280.73	2.991	0.642	0.500	0.300	341.000
2284.15	2.591	0.827	0.480	0.400	350.000
2287.96	2.931	1.288	0.600	0.450	354.000
2292.03	3.331	6.255	1.120	0.600	342.000
2295.83	3.308	0.589	0.470	0.400	356.000
2299.63	3.667	0.765	0.470	0.570	349.000
2301.63	3.618	0.391	0.120	0.360	335.000
2305.44	4.255	1.013	0.420	0.620	346.000
2309.54	2.162	7.998	0.330	0.830	337.000
2313.36	5.469	1.395	0.760	0.710	353.000
2317.17	5.119	0.596	0.110	0.280	365.000
2320.92	4.909	0.876	0.500	0.690	344.000
2324.72	6.075	0.615	0.430	0.570	348.000
2327.84	4.238	0.920	0.520	0.660	349.000
2331.65	0.808				
2335.44	0.811				
2340.28	0.390				
2344.06	0.378				
2347.75	0.366				
2351.57	0.332				
2354.93	0.458				

2358.82	0.216				
2362.62	0.496				
2366.17	4.193	3.474	1.020	0.700	350.000
2369.94	3.446	4.745	0.940	0.630	347.000
2373.50	3.702	2.111	0.890	0.600	348.000
2377.25	2.002	0.097	0.100	0.250	362.000
2381.07	3.178	0.147	0.080	0.260	
2384.34	5.783	1.053	0.650	0.540	353.000
2388.16	7.745	1.094	0.730	0.530	356.000
2392.12	4.366	0.194	0.240	0.510	520.000
2395.92	4.244	1.940	0.590	0.650	344.000
2399.73	4.574	1.123	0.540	0.570	345.000
2404.29	0.841				
2408.13	0.140				
2411.53	0.243				
2415.37	0.240				
2419.40	0.181				
2198.00	1.522	1.067	0.410	0.570	350.000
2213.60	2.556	0.400	0.180	0.280	339.000
2233.01	2.437	0.683	0.320	0.430	339.000
2301.63	3.757	1.109	0.590	0.510	344.000
2305.44	4.411	2.632	1.050	0.620	351.000
2373.50	3.854	2.929	0.930	0.590	347.000
2384.34	6.054	1.338	0.870	0.550	350.000

Depth (m)	PHIg (%)	Depth (m)	PHIg (%)	Depth (m)	PHIg (%)
2181.79	1.15	2257.55	2.06	2340.28	1.54
2190.74	1.43	2261.34	1.21	2344.06	1.37
2198.00	2.32	2265.32	3.26	2347.75	1.61
2204.57	1.93	2273.13	4.09	2354.93	1.68
2207.00	2	2280.73	6.94	2362.62	1.33
2210.30	2.14	2284.15	1.28	2366.17	2.37
2213.60	2.93	2292.03	6.93	2373.50	3.71
2216.98	3.63	2295.83	4.04	2377.25	2.61
2220.30	3.21	2299.63	8.11	2381.07	1.97
2223.58	2.68	2301.63	6.64	2384.34	3
2229.73	2.99	2309.54	1.09	2388.16	5.48
2233.01	2.45	2313.36	9.92	2392.12	5.51
2237.55	3.59	2317.17	7.32	2395.92	6.29
2241.33	1.54	2320.92	8.52	2399.73	5.17
2245.16	2.55	2324.72	6	2404.29	3.37
2250.10	2.49	2327.84	6.25	2408.13	1.56
2253.90	1.85	2331.65	6.01		

References

Anderson, W. (1986, November 1). Wettability Literature Survey- Part 2: Wettability Measurement. Society of Petroleum Engineers. doi:10.2118/13933-PA

Asquith, G., and D. Krygowski, 2004, Basic Well Log Analysis: AAPG Methods in Exploration 16, p.31-35

Bear, J., 1972. Dynamics of Fluid in Porous Media. Dover, New York.

Chalmers, G.R.L., Bustin, R.M., 2008. Lower Cretaceous gas shales in northeastern British Columbia, Part I: geological controls onmethane sorption capacity. Bulletin of Canadian Petroleum Geology 56, 1–21.

Chalmers, G.R.L., D.J.K. Ross,, and R.M. Bustin. 2012.. Geological controls on matrix permeability of Devonian Gas Shales in the Horn River and Liard basins, northeastern British Columbia, Canada. *International Journal of Coal Geology*, 103: 120–131.

Chen, J., Li, B., Georgi, D., Yang, W., and Chen, J. (2012). Petrographic Features of Kerogen in Gas Shales and their Effect on Hydrocarbon Storage. (Society of Petroleum Engineers).

Curtis, M. E., Ambrose, R. J., & Sondergeld, C. H. (2010, January 1). Structural Characterization of Gas Shales on the Micro- and Nano-Scales. Society of Petroleum Engineers. doi:10.2118/137693-MS

Dong, T., Kennedy, M. 2014. Geochemical Characterization of Stratigraphic Sequences in the Horn River Shale, Middle and Upper Devonian, Northeastern British Columbia, Canada. Presented at the AAPG Annual Convention and Exhibition held in Pittsburgh, Pennsylvania, May 19-22, 2013. AAPG (2013)

Dong, T., Harris, N.B., Ayranci, K., Twemlow, C.E. and Nassichuk, B.R., 2015. Porosity characteristics of the Devonian Horn River shale, Canada: insights from lithofacies classification and shale composition. *International Journal of Coal Geology*, *141*, pp.74-90.

Ewing, R.P., Horton, R., 2002. Diffusion in sparsely connected pore spaces: temporal and spatial scaling. Water Resources Research 38 (12), 1285.

Ewing, R. P.; Hu, Q.; Liu, C.Scale dependence of intragranular porosity, tortuosity, and diffusivity. Water Resour. Res. 2010, 46, W06513; doi:, DOI: 06510.01029/02009WR008183.

Hager, J. (1998), Steam drying of porous media, PhD thesis, Department of Chemical Engineering, Lund Univ., Sweden.

Harris, N. B., and T. Dong, 2013, Characterizing porosity in the horn river shale, northeastern British Columbia. BC Ministry of Energy and Mines, Oil & Gas Report.

Hjelmeland, O.S. and Larrondo, L.E.: "Experimental Investigation of the Effects of Temperature, Pressure, and Crude Oil Composition on Interfacial Properties," SPEFE (July 1986) 321-28.

Hu, Q.H. Integrated Experimental and Modeling Approaches to Studying Fracture-Matrix Interactions in Gas Recovery from Barnett Shale. Presented at the Research Partnership to Secure Energy for America held in Canonsburg, Pennsylvania, USA, 17-18 April, 2012. RPSEA (2012)

Hu, Q., and R. Ewing. 2014. Integrated experimental and modeling approaches to studying the fracture-matrix interaction in gas recovery from Barnett Shale. Final Report, Research Partnership to Secure Energy for America (RPSEA), National Energy Technology Laboratory, Department of Energy, 91p.

Hu, Q.H., Gao, X.B., Gao Z.Y., Ewing, R.P., Dultz, S., Kauffman, J.. Pore Accessibility and Connectivity of Mineral and Kerogen Phases in Shales. Presentation at the Unconventional Resources Technology Conference held in Denver, Colorado, USA, 25–27 August 2014. URTeC 1922943, (2014).

Hu, Q.H., R.P. Ewing, and H.D. Rowe. 2015. Low nanopore connectivity limits gas production in Barnett Formation. *Journal of Geophysical Research – Solid Earth*, 120(12): 8073–8087.

Jarvie, D.M., 2012. Shale resource systems for oil and gas: Part 2—Shale-oil resource systems.

Katz, B. J., 1983, Limitations of 'Rock-Eval' pyrolysis for typing organic matter: Organic Geochemistry, 4, 195-199.

Kaufmann, J. 2010. Pore space analysis of cement-based materials by combined nitrogen sorption - Wood's metal impregnation and multi-cycle mercury intrusion. Cement Concrete Comp. 32(7): 514-522.

Katz, A. J., and A. H. Thompson, 2016. Quantitative prediction of permeability in porous rock, Phys. Rev. B., 34, 8179 – 81.

Khan S, Ansari S, Khosravi N., et al. Understanding shale heterogeneity – key to minimizing drilling problems in Horn River Basin. Proceedings IADC/SPE Drilling Conference and Exhibition, 2012. Paper IADC/SPE 151752.

Kiepsch, S. and Pelster, R., 2016. Interplay of vapor adsorption and liquid imbibition in nanoporous Vycor glass. *Physical Review E*, *93*(4), p.043128.

King HE, Eberle APR, Walters CC, Kliewer CE, Ertas D, Huynh C, 2015. Pore architecture and connectivity in gas shale. Energy Fuels 29:1375–1390

Kuila U, Prasad M, Derkowski A, McCarty DK. 2012. Compositional controls on mudrock pore-size distribution: an example from Niobrara formation. In SPE Annual Technical Conference and Exhibition January 1, 2012. Society of Petroleum Engineers.

Lan, Q.,Xu, M., Binazadeh, M., Dehghanpour, H., Wood, J.M., A comparative investigation of shale wettability: The significance of pore connectivity, Journal of Natural Gas Science and Engineering, Volume 27, Part 2, November 2015, Pages 1174-1188, ISSN 1875-5100, http://dx.doi.org/10.1016/j.jngse.2015.09.064.

Langford, F.F. and Blanc-Valleron, M.M., 1990. Interpreting Rock-Eval pyrolysis data using graphs of pyrolizable hydrocarbons vs. total organic carbon (1). *AAPG Bulletin*, *74*(6), pp.799-804.

Larionov, V. V. (1969), Radiometry of boreholes (in Russian), NEDRA, Moscow

Leckie, D.A., (1992). Regional Setting, Evolution and Depositional Cycles of the Western Canada Foreland Basin. In: Macqueen R.W., Leckie, D.A. (eds) Foreland Basins and Fold Belts. AAPG Memoir 55: 9-46

Levson, V., Walsh, W., Adams, C., Ferri, F., and Hayes, M., 2009, An Overview of Shale Gas Potential in Northeastern British Columbia. Presented at the 2009 CSPG CSEG CWLS Convention, May 4 to May 8, Calgary, Alberta, Canada, http://www. geoconvention.org/2009abstracts/236.pdf, downloaded Jun. 22, 2009

Loucks, R. G., Reed, R. M., Ruppel, S. C., and Jarvie, D. M., 2009. Morphology, Genesis, and Distribution of Nanometer-Scale Pores in Siliceous Mudstones of the Mississippian Barnett Shale, Jour. Sedimentary Research 79, p. 848-861.

MacLean, B.C., and D.W. Morrow, 2004, Bovie structure: Its evolution and regional context. *Bulletin of Canadian Petroleum Geology*, 52: 302–324.

Mason EW. 1994. Subsurface Structural Analysis of the Deep Basin, Alberta, Canada. UMI Publishing (1) [1994, cited 2016 May]

McPhail, S., Walsh, W., Lee, C. and Monahan, P.A. (2008): Shale units of the Horn River Formation, Horn River Basin and Cordova Embayment, northeastern British Columbia; British Columbia Ministry of Energy, Mines and Natural Gas, Petroleum Geology Open File Report No. 2008-1, 14 pages.

Mossop, G.D. and Shetsen, I. (comps), 1994. Geological Atlas of the Western Canada Sedimentary Basin. Calgary, Canadian Society of Petroleum Geologists and Alberta Research Council, 510p.

Nieto, J., Bercha, R., & Chan, J. (2009, January). Shale Gas Petrophysics-Montney and Muskwa, Are They Barnett Look-Alikes?. In SPWLA 50th Annual Logging Symposium. Society of Petrophysicists and Well-Log Analysts.

Passey, Q.R., Creaney, S., Kulla, J.B., Moretti, F.J. and Stroud, J.D., 1990. A practical model for organic richness from porosity and resistivity logs. *AAPG bulletin*, *74*(12), pp.1777-1794.

Passey, Q. R.; Bohacs, K. M.; Esch, W. L.; Klimentidis, R.; Sinha, S. International Oil and Gas Conference and Exhibition in China, Beijing, China, June 8−10, 2010; Society of Petroleum Engineers: Kuala Lumpur, Malaysia, 2010; SPE Paper No. 131350.

Philip, J.R., 1957. The theory of infiltration: 4. Sorptivity and algebraic infiltration equations. Soil Sci. 84, 257–265.

Reynolds, M. M., & Munn, D. L. (2010, January 1). Development Update for an Emerging Shale Gas Giant Field - Horn River Basin, British Columbia, Canada. Society of Petroleum Engineers. doi:10.2118/130103-MS

Rivard, C.; Lavoie, D.; Lefebvre, R.; Séjourné, S.; Lamontagne, C.; Duchesne, M. An overview of Canadian shale gas production and environmental concerns. Int. J. Coal Geol., 2013, in press (http://dx.doi.org/10.1016/j.coal.2013.12.004).

Ross, D.J.K., Bustin, R.M., 2008. Characterizing the shale gas resource potential of Devonian-Mississippian strata in the Western Canada sedimentary basin: application of an integrated formation evaluation. AAPG Bull. 92, 87–125.

Ross, D.J.K.; Bustin, R.M. 2009. The Importance of Shale Composition and Pore

Structure Upon Gas Storage Potential of Shale Gas Reservoirs. Petroleum Geology, 26, 916−927.

Sigal RF, Qin B. Examination of the importance of self diffusion in the transportation of gas in shale gas reservoirs. Petrophysics 2008;49:301–5.

Stauffer, D., Aharony, A., 1994. Introduction to Percolation Theory, 2nd ed. Taylor and Francis, London.

Thyne, G. D., 2013, A review of the measurement of wettability in shales. Technical Report, DOI: 10.13140/RG.2.14568.0806.

Vincent, O., Marguet, B. and Stroock, A., 2016. Imbibition triggered by capillary condensation in nanopores. *arXiv preprint arXiv:1612.06684*.

Volpi, V., Camerlenghi, A., Hillenbrand, C.-D., Rebesco, M., Ivaldi, R., 2003. Effects of biogenic silica on sediment compaction and slope stability on the Pacific margin of the Antarctic Peninsula. Basin Res. 15, 339–363.

Wang, S., F. Javadpour, and Q.H. Feng. 2016. Confinement correction to mercury intrusion capillary pressure of shale nanopores. *Scientific Reports*, 6: 20160, doi: 10.1038/srep20160.

Washburn, E. W., 1921. Note on a Method of Determining the Distribution of Pore Sizes in a Porous Material: Proceedings of the National Academy of Sciences, 7(4): 115–116, doi:10.1073/pnas.7.4.115.

Webb, P. A. (2001), An introduction to the physical characterization of materials by mercury intrusion porosimetry with emphasis on reduction and presentation of experimental data, 23 pp., Micromeritics Instrument Corporation, Norcross, Ga.

Wignall, P.B., Newton, R., 2003. Contrasting deep-water records from the Upper Permian and Lower Triassic of South Tibet and British Columbia: evidence for a diachronous mass extinction. Palaios 18, 153–167

Williams, G. K., 1983, What does the term Horn River Formation mean?: Bulletin of Canadian Petroleum Geology, v. 31, p. 117– 122.6

Yang, L., Ge, H., Shen, Y., Ren, K., Sheng, M., Gao, Z., Qin, X. and Su, S., 2015, November. Experimental Research on the Shale Imbibition Characteristics and Its Relationship with Microstructure and Rock Mineralogy. In *SPE Asia Pacific Unconventional Resources Conference and Exhibition*. Society of Petroleum Engineers.

Yuan W., Pan Z., Li X., et al. Experimental study and modelling of methane adsorption and diffusion in shale. Fuel, 117 (2014), pp. 509–519

Biographical Information

Tony Sortore was born in Lavan, TX and raised in Fort Worth, TX. He is a first generation college student and 3rd generation United States citizen. He attended R.L. Paschal High School in Fort Worth and proceeded to initially study music at the University of Oklahoma and Dallas Baptist University. After deciding to study geology at The University of Texas at Arlington he avidly participated in the college's organizations during both his undergraduate and graduate programs. While obtaining his masters he obtained two internships and competed in the school's Imperial Barrel Award team which won 3rd place in regionals.